Validation of Volumetric Contact Dynamics Models

by

Michael Boos

A thesis
presented to the University of Waterloo
in fulfillment of the
thesis requirement for the degree of
Master of Applied Science
in
Systems Design Engineering

Waterloo, Ontario, Canada, 2011

I hereby declare that I am the sole author of this thesis. This is a true copy of the thesis, including any required final revisions, as accepted by my examiners.

I understand that my thesis may be made electronically available to the public.

Abstract

A volumetric contact dynamics model has been proposed by Gonthier et al. [1, 2, 3] for the purpose of rapidly generating reliable simulations of space-based manipulator contact dynamics. By assuming materials behave as a Winkler elastic foundation model, forces and moments between two bodies in contact can be expressed in terms of the volume of interference between the undeformed geometries of the bodies. Friction between bodies is modelled by a dwell-time dependent bristle model for both tangential friction, and spinning friction torque.

This volumetric model has a number of advantages. Unlike point-contact models, it allows for the modelling of contact between complex geometries and scenarios where the contact surface is relatively large, while being less computationally expensive than finite element methods. Rolling resistance is included in the model through damping effects across the volume of interference. The friction model accounts for dwell-time dependent slip-stick effects, spinning friction torque, and the Contensou effect. In this thesis, an experimental validation of the volumetric contact model is presented for the first time.

Models for simple geometries in contact (e.g. cylinder-on-plane, sphere-on-plane) have been developed for stationary contact and for contact with motion normal and tangential to the contact surface. Tangential motion is modelled with pure translation, pure rotation about the normal axis, and combined motion, in order to separately consider friction forces, spinning friction torque, and the Contensou effect, respectively.

An apparatus has been developed to experimentally validate these models for metal-on-metal contact. The apparatus has two configurations, one for validating the normal contact models and the other for the friction models. Experimental measurements of forces and displacements are used to identify model parameters (e.g. volumetric stiffness, friction coefficients, etc.).

For normal force experiments, modelling the contact forces as proportional to volume of interference was found to be a reasonable approximation. A Hertzian model was compared with the volumetric model for spherical payloads loaded quasi-statically. Using stiffnesses estimated from spherical experiments, small misalignments of the cylindrical payloads were estimated that corresponded well with measured results. Dynamic experiments suggest an inverse relationship between impact velocity and the hysteretic damping coefficient.

The high normal forces applied in the friction experiments were found to create significant wear on the contact surfaces. Coefficients of friction between titanium and aluminum were found to be consistent translationally and rotationally. Friction forces from combined translation and rotation demonstrate that the Contensou effect is accurately described by the volumetric contact model.

Acknowledgements

I would like to thank my supervisor Prof. John McPhee, Dr. Yves Gonthier, the Canadian Space Agency, Parallel Geometry, and NSERC for providing this project and for their support of my work.

I would also like to thank my colleagues in the Motion Research Group for their help and company, especially Matt, Willem, Aden, and Joydeep.

My roommates Aaron and Dave have been especially supportive and accommodating in my final push to finish this document.

Dedication

I would like to dedicate this thesis to my fiancée, Kandace. Thanks for all your encouragement and support to finish this. I am very much looking forward to having you by my side for the next one!

Contents

List of Tables

List of Figures

Chapter 1

Introduction

1.1 Background and Motivation

The Mobile Servicing System (MSS), Canada's main contribution to the International Space Station (ISS), consists of two robotic manipulators, the Space Station Remote Manipulator System (SSRMS) and the Special Purpose Dextrous Manipulator (SPDM). The MSS is used for assembly and maintenance of the ISS [4]. Tele-operated space-based robotic operations require careful task planning, verification and training on the ground. The complexity and risk of these operations means that accurate real-time contact dynamics models are required for on-earth simulation and astronaut training.

Many point contact models are unsuitable for situations involving complex or conforming contacts, which may occur when handling orbital replacement units such as battery packs. More complex models, such as finite element models, are too computationally intensive for real-time simulation. The Canadian Space Agency has applied hardware-in-the-loop simulations (HLS) to determine contact dynamics; however HLS can be expensive and very difficult to implement [5].

A volumetric contact model has been proposed by Gonthier et al. [1] for generating reliable simulations of space-based manipulator operations. This model is applicable to complex and conforming geometries, and accounts for angular dynamics ignored by many point contact models, including rolling resistance and spinning friction torque. However, experimental validation of this model is required.

1.2 Contact Modelling

1.2.1 Normal forces

Contact is often modelled using *point-contact* models — that is, the region of contact is assumed to be very small relative to the geometries of the bodies, such that contact may be assumed to occur at a single point. A common model used in relatively stiff contact for robot modelling is the Kelvin-Voigt model, in which the contacting materials are represented by a spring and damper in parallel [6], for which the normal force is given by

$$f_N = K(\delta) + B(\dot{\delta}) \tag{1.1}$$

where δ and $\dot{\delta}$ are the depth of penetration and rate of penetration of the geometries (as depicted in Figure 1.1), and K and B are the stiffness and damping functions. However, there are a number of limitations stemming from the damper including 'stickiness' during lift-off and a discontinuous force at impact due to a non-zero normal velocity [7].

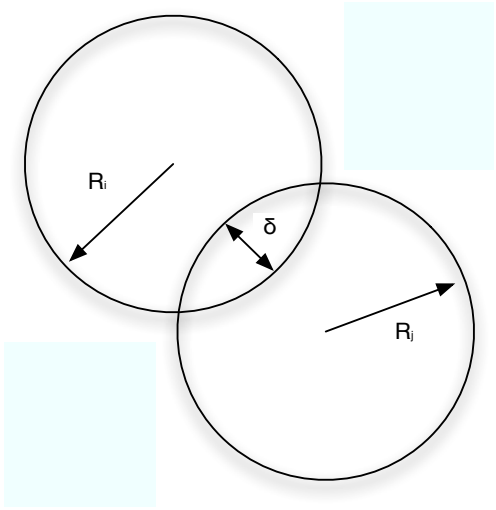

Figure 1.1: Depth of penetration δ between two spheres in contact.

The contact model proposed by Hunt and Crossley is a normal force model similar to spring-damper models, where the spring force is based on Hertz theory for linear elastic solids and the damping is adjusted to avoid the limitations incurred by other models. The Hertz model for contact force is the best known model for contact between two spheres

of isotropic material [8]. To use this model, two assumptions must be made [1]. First, it must be assumed that the contact patch is small relative to the geometries of the bodies. This allows contact to be considered from a single point, where the depth of penetration δ can be measured. Consequently, the surfaces must be non-conforming (i.e. not concave relative to each other where they come into contact). Otherwise, contact might occur at more than one location or be spread out over a wide area. Secondly, it is assumed that the bodies are homogeneous isotropic, linearly elastic solids.

According to Hertz theory, the contact normal force is given by

$$f_N = k\delta^n \tag{1.2}$$

The generalized stiffness k is dependent on the shapes and material properties of the surfaces in contact. For two spheres in contact, $n = \frac{3}{2}$.

The Hertz theory formulation is applicable for spheres in contact under static conditions. If pure Hertz theory were to be applied for dynamic contact situations (ignoring friction), no energy would be dissipated in the process of contact. Thus some damping is necessary [8].

Hunt and Crossley [9] adapted the Kelvin-Voigt model of Equation (1.1), proposing the following model for the contact normal force:

$$f_N = K(\delta) + B(\dot{\delta}, \delta) \tag{1.3a}$$

$$= k\delta^n + (\lambda\delta^n)\dot{\delta} \tag{1.3b}$$

where λ is the hysteretic damping factor. Equation (1.3b) is consistent with Hertzian theory for contacting spheres under static conditions for $n = \frac{3}{2}$.

For low impact velocities and most linear elastic materials [10], the coefficient of restitution can be approximated for a limited range of values by

$$e = 1 - \alpha v_i \tag{1.4}$$

where α is an empirically determined value and v_i is the initial impact speed. Marhefka and Orin showed [7] that

$$f_N \approx k\delta^n(1 + \frac{3}{2}\alpha\dot{\delta}) \tag{1.5}$$

However, the α parameter only holds for a limited range of impact velocities. Thus, the model is limited only to scenarios with low impact velocites [11], such as those associated with space robotic tasks [1].

Point contact models like Hunt-Crossley are fast and efficient; little effort is required to compute the penetration depth and rate for simple geometries, as well as the contact forces. In addition, the model is continuous in velocities and accelerations, which aids numerical integration and should not introduce discontinuous disturbances for control. The static contact force in this particular model is based on physical theory, yielding high fidelity for low-speed impact and where assumptions about the size and shape of the contact region hold.

However, not all contact scenarios involve relatively small contact patches or simple, non-conforming geometries. In these cases, other models are required to accurately simulate contact. In addition, point contact models ignore the rotational effects of contact. A complete contact model should account for torques derived from rolling resistance and spinning friction.

A volumetric contact model has been proposed by Gonthier et al. [1, 2, 3]. Normal contact forces depend on the volume of interference between the undeformed geometries of the bodies, which allows a wide variety of contact geometries to be accounted for. The model also is shown to naturally account for rolling resistance torque. This model is described in detail in Chapter 2.

1.2.2 Friction forces

Once normal forces are determined, sliding friction forces are often characterized by a Coulomb model,

$$f_t = \mu f_n \tag{1.6}$$

where μ is the friction coefficient. Many dry friction models consider two primary regimes dependent on the relative speed of the bodies, sticking and slipping [12], shown in Figure 1.2. During the sticking phase, forces build up to a maximum rate μ_s, the static coefficient of friction, at which point slipping begins to occur. Slipping friction for dry friction models settles to a constant rate of μ_d, the dynamic coefficient of friction.

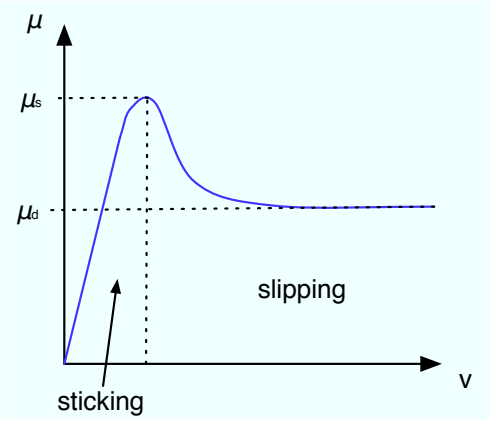

Figure 1.2: Friction coefficient as a function of velocity.

While friction forces are still poorly understood [13], it is generally accepted that dry friction results from interference between the surface asperities and roughness of the bodies, as well as molecular attractions [14, 15]. This helps to understand conceptually how sticking and slipping occur. At rest, asperities between two bodies will begin to interlock with each other. As forces are applied that would cause the bodies to slide over each other, these asperities will begin to deflect. Static friction forces are the resistance to this deflection. Finally, slipping occurs as the asperities break free of each other, and the lesser dynamic sliding friction is a consequence of these asperities pushing past each other.

Lubricated friction models must account for the viscous effects of the fluid between the surfaces. Armstrong-Helouvry et al. [16] identify four regimes in lubricated friction. The first, stiction, corresponds to the stiction regime in dry friction. The second regime, boundary lubrication, takes place as surface asperities are beginning to break free of each other, but the velocity is insufficient for the lubricant to form a fluid film between the surfaces. The lubricant between asperities will lead to a reduction in friction force called the Stribeck effect. Third, the partial fluid lubrication regime takes place when a film between the surfaces begins to form, but there is still contact between asperities. In the fourth regime, full-fluid lubrication takes place when there is no solid contact between the bodies, and resistance to motion is entirely viscous damping.

A point-contact friction model that accounts for the sticking and slipping of dry friction through a bristle model, as well as lubricated viscous friction, was developed by Gonthier et al. [5]. This model also includes a dwell-time dependency to describe the tendency for

the maximum stiction force to be greater over time when bodies in contact have been at rest [16].

Point-contact models can reasonably model friction if motion is purely tangential, but they do not describe the friction torque that would resist spinning motions over the contact surface area. In addition, they do not account for the phenomena discovered by Contensou [17], where tangential and spinning friction are not independent, but tangential friction may decrease as angular velocity is increased. This effect can be observed in the reduced force required to push a floor polisher or sander while spinning. As a part of the volumetric contact model, Gonthier et al. [2] developed a model for describing both tangential friction force and spinning friction torque in terms of an average surface velocity that accounts for both lateral and spinning motion.

Gonthier has combined the tangential dwell-time dependent bristle friction model into the volumetric model to provide a comprehensive volumetric friction contact model [1] which is described in detail in Chapter 4.

1.3 Experimental Validation and Parameter Identification of Contact Models

Hertz contact theory has been well-established experimentally [10]. As the theory was developed to study contact between lenses [18], the interference patterns created by lenses in contact have been used to demonstrate its validity.

Due to its simplicity, a linear Kelvin-Voigt model, given by

$$f_n = k\delta + b\dot{\delta} \tag{1.7}$$

is frequently used in manipulator modelling [19, 20, 21]. Agar used this model to estimate linear stiffness parameters for a variety of payload shapes made from both aluminum and plastic [20]. Experimental results were gathered using a six degree-of-freedom serial manipulator over a force plate and compared against measurements taken from an Instron machine. Differences between contact stiffness estimates revealed a high amount of error stemming from machine compliances and position repeatability, estimator convergence problems, and datum estimation.

Verscheure et al. performed similar experiments using a plastic sphere, a plastic cone, a plastic pyramid, and an aluminum sphere [22], but identified parameters for a Hertzian model, given by Equation (1.2). Using a row-wise total least squares estimation algorithm, he found results that were consistent between the serial manipulator, the Instron machine, and finite element contact models.

Diolaiti et al. performed experiments for parameter identification with both a linear Kelvin-Voigt model and the Hunt-Crossley model with stiff polycarbonate and a silicon gel [21]. A half-sphere was driven into the contact material with a sinusoidal motion. An online recursive estimator was used to estimate contact parameters for the models. The linear model did not provide good characterization of the flexible gel, but for the stiffer polycarbonate, both the linear and Hunt-Crossley models were adequate.

For measuring stick-slip friction, a common setup is depicted in Figure 1.3. A slider is attached to a fixed wall with a spring [13] or both a spring and damper in parallel [16]. The slider rests on a platform or conveyor underneath that moves away from the wall at a set velocity.

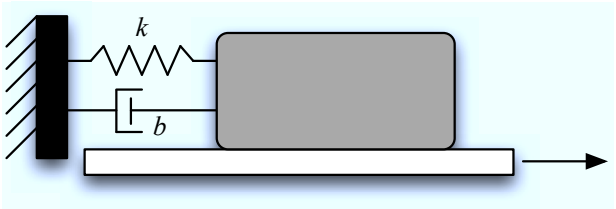

Figure 1.3: Slip-stick experiment.

For low speeds, the slider will oscillate as the conveyor repeatedly drags the slider far enough such that the spring force exceeds the maximum friction force and it recoils. When the speed of the slider matches the conveyor, it will stick and be dragged forward again. Knowing the stiffness of the spring, the maximum stiction friction can be estimated based on the distance the slider is dragged before it is first pulled back. As the speed is increased, the frequency of the oscillations will increase, while their magnitude will decrease due to dwell-time dependency, as the slider has less time to stick to the conveyor. Eventually, oscillations will cease entirely and the slider will slip continuously at a point where the spring and kinetic friction forces are equally opposed.

Liang et al. extended this basic setup for testing a two-dimensional bristle model [23].

A slider is placed on the edge of a turntable and mounted to orthogonal walls by two springs, shown in Figure 1.4. This allowed for consideration of the bristles on the contact surface deflecting in more than one direction. However, the slider rotates slightly about one corner as it is dragged, and the model considered did not account for any spinning friction torque or rotational effects that might occur on a rotating platform.

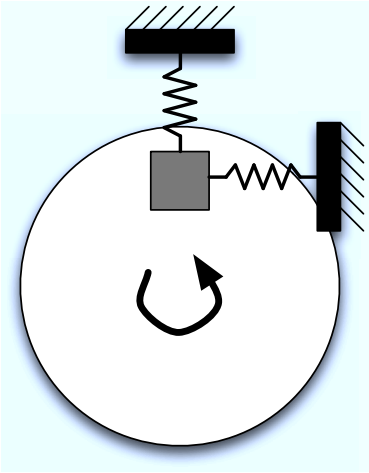

Figure 1.4: 2D bristle model slip-stick experiment.

Liang et al. also tested this 2D bristle model by launching a slider horizontally at a set velocity over an inclined plane. The slider was pulled down the plane by gravity and eventually slowed by friction before coming to rest. The simulation accurately predicted the observed forces and stopping point.

Gonthier outlines some possible methods for friction parameter identification in his thesis [1]. These methods are discussed in Chapter 5.

1.4 Contributions

The volumetric contact model proposed by Gonthier et al. [1, 2, 3] requires experimental validation. The model must be demonstrated to describe real-world phenomena in order to be used in simulation. In addition, since several model parameters cannot be derived directly from theoretical material properties, experiments to identify these parameters are required.

While simple point contact models relating force to penetration depth have been validated for certain robotic operations, no other work to date has experimentally investigated contact models where the normal force is proportional to volume of interference. Likewise, while some aspects of the volumetric friction model such as bristle stiffness and coefficients of friction have already been demonstrated experimentally by others, aspects of the model that describe phenomena such as spinning friction torque and the Contensou effect have yet to be tested.

This work presents a series of experiments designed to measure contact model parameters and to test and demonstrate the features of the model. Specifically, hard metal-on-metal contact is investigated, as these materials are used in both spacecraft manipulators and payloads, and will need to be simulated. An apparatus has been developed to experimentally validate these models for contact between metals.

Experiments have been divided into those pertaining to normal forces and friction forces. Chapter 2 outlines the volumetric contact normal force model. Experiments to validate this aspect of the model are described in Chapter 3, along with the results of those experiments. The volumetric friction model is presented in Chapter 4. Chapter 5 outlines experiments for validating models for friction force, spinning friction torque, and the Contensou effect.

Chapter 2

Normal Volumetric Contact Model

2.1 Introduction

A flexible volumetric contact dynamics model has been proposed by Gonthier et al. [3]. This model allows for more complex and conforming geometries where point contact models may be inadequate because contact surfaces are relatively large, or where closed-form solutions from elastic theory are not available. It can be shown that the model also accounts for angular dynamics such as rolling resistance and spinning friction torque.

For larger or conforming contact surfaces, a Winkler elastic foundation model [18] has been used. The Winkler model assumes a pressure distribution from one surface deforming as a 'bed of springs' to comply with the contacting surface. This model has been adapted to contact dynamics; the forces and moments between two bodies in contact can be expressed directly in terms of the volume of interference, V, between the undeformed geometries of the bodies.

There are two methods of representing deformations in the volumetric model. The first is a one-body deformation model, where one body is assumed solid and the other deformable, as depicted in Figure 2.1. In this model, the contact surface is the outer surface of the second solid body. The second, the two-body deformation model, assumes both bodies are compliant. In this case, the contact surface lies somewhere between the two solid geometries, in the volume of interference, and is dependent on the relative stiffnesses of the objects.

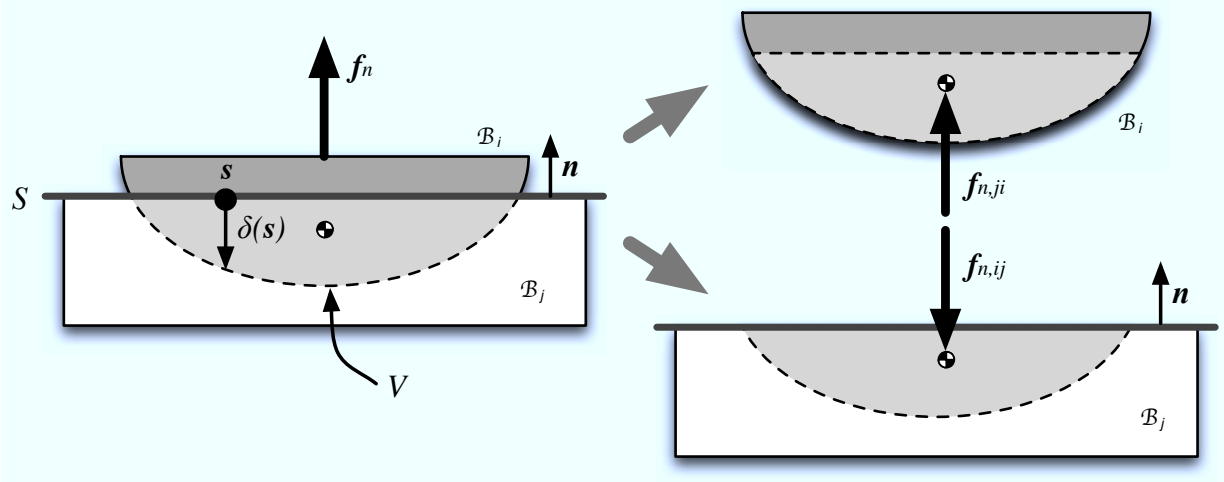

Figure 2.1: Volume of interference between two contacting bodies in a one deformable body model.

2.2 One Deformable Body Contact Model Properties

In a one deformable body contact model, one of the bodies, $\mathcal{B}_i$ is flexible, while the other, $\mathcal{B}_j$ is perfectly rigid. The contact surface S is assumed to be a flat surface on $\mathcal{B}_j$.

The volume of interference, that is, the volume $\mathcal{B}_i$ is compressed by, is given by

$$V = \int_S \delta(\mathbf{s}) dS = \int_V dV \tag{2.1}$$

where S is the contact surface and $\delta(\mathbf{s})$ is the depth of penetration at point $\mathbf{s}$ on the contact surface, as depicted in Figure 2.1. The vector $\mathbf{n}$ is defined as unit vector normal to S.

The centroid of this volume is

$$\mathbf{p}_c = \frac{1}{V} \int_V \mathbf{p}\, dV \tag{2.2}$$

where $\mathbf{p}$ is the position vector to a point in the volume.

The weighed surface centroid $\mathbf{s}_c$ is given by

$$\mathbf{s}_c = \frac{1}{V} \int_S \mathbf{s}\, \delta(\mathbf{s}) dS\ . \tag{2.3}$$

Gonthier demonstrates that the volumetric and surface centroids are collinear along the unit vector $\mathbf{n}$ [1].

Another relevant property is the contact surface second moment of area, $\mathbf{J}_s$, weighted by penetration depth:

$$\mathbf{J}_s = \int_S \left[(\boldsymbol{\rho}_s \cdot \boldsymbol{\rho}_s)\mathbf{I} - \boldsymbol{\rho}_s\boldsymbol{\rho}_s\right] \delta(\mathbf{s}) dS \tag{2.4}$$

where $\boldsymbol{\rho}_s$ is a vector from the centroid $\mathbf{p}_c$ to the point $\mathbf{s}$ on the surface and $\mathbf{I}$ is the identity matrix. This can be approximated by the volume inertia tensor

$$\mathbf{J}_s \approx \mathbf{J}_V = \int_V \left[(\boldsymbol{\rho}_V \cdot \boldsymbol{\rho}_V)\mathbf{I} - \boldsymbol{\rho}_V\boldsymbol{\rho}_V\right] dV \tag{2.5}$$

where $\boldsymbol{\rho}_V$ is a vector from the centroid $\mathbf{p}_c$ to the point $\mathbf{p}$ in the volume. Inertia tensor $\mathbf{J}_V$ is easier to calculate for arbitrary geometries.

2.3 Normal Force

In this model, contact pressure is proportional to the depth of penetration at each point on the surface S. Integrating over S, the contact normal force is related directly to the size of the volume of interference through a volumetric stiffness k_V, given in units of force per unit volume. The normal force is given by [3]

$$\mathbf{f}_N = k_V V(1 + a v_{cn})\mathbf{n} \tag{2.6}$$

where a is a hysteretic damping parameter and v_{cn} is the relative speed of the bodies in the normal direction $\mathbf{n}$, measured at the centroid $\mathbf{p}_c$. This force acts normal to the contact surface, through the centroid of the volume.

It should be noted that Equation (2.6) is very similar in form to Equation (1.5) for the point-based Hunt-Crossley model. For free collision, the parameter a can be shown to depend on only the coefficient of restitution, e, and the initial impact velocity, v_{cn}^i [5]:

$$a = \frac{d}{e v_{cn}^i} \tag{2.7}$$

where d is related to e by

$$\frac{1 + d/e}{1 - d} = e^{d(1+1/e)} \tag{2.8}$$

or which can be approximated as,

$$d \approx 1 - e^2 \, . \tag{2.9}$$

2.4 Rolling Resistance Torque

As motion in the normal direction is damped through the normal contact force, there will also be resistance to tangential rolling, as tangential rolling causes parts of the contact surface to move in the normal direction. Gonthier et al. [3] found that by integrating the contact pressure distribution over the contact surface, the rolling resistance torque is

$$\boldsymbol{\tau}_r = k_V a \, \mathbf{J}_S \cdot \boldsymbol{\omega}_t \tag{2.10}$$

where $\boldsymbol{\omega}_t$ is the component of the relative angular velocity between the bodies tangent to the contact surface. This gives an expression for rolling resistance torque without the need to introduce any new parameters to describe resistance to rolling.

2.5 Two Deformable Body Contact Model Extension

The one deformable body model can be extended so that both bodies in contact undergo some deformation. In this case, the contact surface cannot be derived from the surface of one of the bodies, but divides the volume of interference, as in Figure 2.2. The contact surface is assumed to be an imaginary flat rigid plane between the two bodies with normal vector $\mathbf{n}$.

On either side of the contact surface are the volumes of interference for each body, V_i and V_j:

$$V_i = \int_S \delta_i(\mathbf{s}) dS \ , \ V_j = \int_S \delta_j(\mathbf{s}) dS \tag{2.11}$$

where $\delta_i(\mathbf{s})$ and $\delta_j(\mathbf{s})$ are the penetration depths of each body past the contact surface S at point $\mathbf{s}$. The two volumes can be summed to give the total volume of interference, V,

$$V = V_i + V_j \tag{2.12}$$

$$= \int_S \delta(\mathbf{s}) dS \tag{2.13}$$

which is equivalent to Equation (2.1).

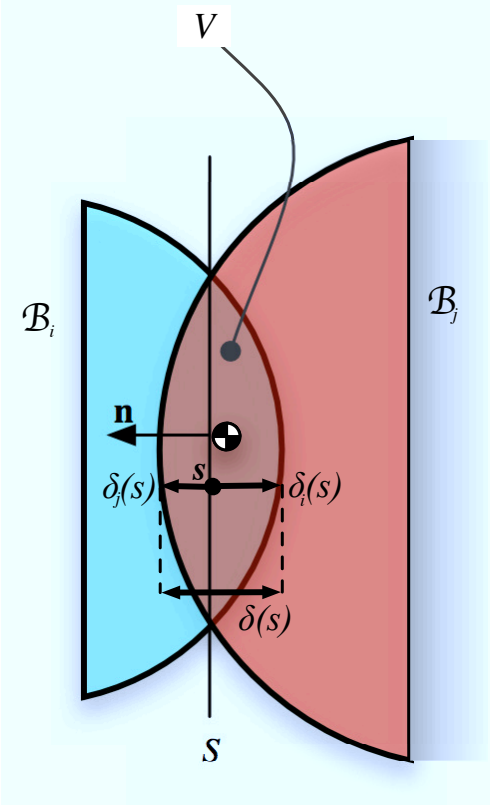

Figure 2.2: Volume of interference between two contacting bodies in a two deformable body model.

The normal forces resisting compression of each body's volume must be equal. Using (2.6), the magnitudes of the contact normal forces in the quasi-static case are

$$f_{N,i} = k_{V,i} V_i \tag{2.14}$$

$$f_{N,j} = k_{V,j} V_j \tag{2.15}$$

where $k_{V,i}V_i$ and $k_{V,j}V_j$ are volumetric stiffnesses of $\mathcal{B}_i$ and $\mathcal{B}_j$, respectively. Since the forces are equal,

$$k_{V,i} V_i = k_{V,j} V_j \ . \tag{2.16}$$

The two volumetric stiffnesses can be combined into a single equivalent stiffness parameter, k_V, in the same manner in which a stiffness can be determined for two linearly elastic springs in series:

$$k_V = \left(\frac{1}{k_{V,i}} + \frac{1}{k_{V,j}} \right)^{-1} \ . \tag{2.17}$$

Using this equivalent stiffness yields a singular expression for the normal force that is the same as Equation (2.6), where $\mathbf{v}_{cn}$ represents the velocity of the bodies relative to each other, measured from the centroid of the contact surface, $\mathbf{s}_c$. This contact point lies at the boundary between the two deformed volumes V_i and V_j and can be shown [1] to be

$$\mathbf{s}_c = \mathbf{p}_c + \left(\frac{k_{v,j} - k_{v,i}}{k_{v,i} + k_{v,j}} \right) \frac{h_V}{2} \mathbf{n} \tag{2.18}$$

where $\mathbf{p}_c$ is the centroid of the entire volume of interference as in Equation (2.2), $\mathbf{n}$ is the normal vector directed away from $\mathcal{B}_i$, and h_V is the average height of the volume measured parallel to $\mathbf{n}$. This height can be determined by

$$h_V = \frac{V}{A_c} \tag{2.19}$$

where A_c is the surface area of S.

Similarly, it can be shown that rolling resistance torque is also identical for both the one and two body deformable cases. The total surface inertia tensor, $\mathbf{J}_s$, is the same as in Equation (2.4), and the rolling resistance torque, $\boldsymbol{\tau}_r$ is given by Equation (2.10).

The normal vector $\mathbf{n}$ defining the orientation of the contact surface is an eigenvector of the volume inertia tensor $\mathbf{J}_V$. This does not necessarily correspond to the normals of either surface.

Gonthier demonstrates that by assuming that the contact plate is a rigid flat surface, no new forces or torques are introduced as compared to other flexible contact plate shapes that also satisfy the constraints of balanced forces [1]. It is also shown that by making one body completely rigid, (i.e. $k_{V,j} \gg k_{V,i}$), the equations governing normal forces and rolling resistance torque are identical to those of the one body deformable model.

2.6 Normal Contact Model Parameters

The parameters of the volumetric normal contact model proposed by Gonthier et al. are listed in Table 2.1.

Parameter	Description	Units
k_V $(k_{V,i}, k_{V,j})$	Volumetric stiffness	N/m^3
a	Damping coefficient (may depend on e for free collision)	s/m
e	Coefficient of restitution	

Table 2.1: Volumetric normal contact model parameters.

Table 2.2 lists model values that must be computed from geometries and measured displacements.

Value	Description	Type	Units
V	Volume of interference	scalar	m^3
$\mathbf{p}_c$	Volume centroid	vector	m
$\mathbf{s}_c$	Surface centroid	vector	m
$\mathbf{J}_s$	Surface inertia tensor	2^{nd} order tensor	m^5
$\mathbf{J}_V$	Volume inertia tensor	2^{nd} order tensor	m^5
$\mathbf{n}$	Normal vector	vector	
v_{cn}	Relative velocity normal to $\mathbf{n}$	scalar	m/s
v_{cn}^i	Initial impact velocity normal to $\mathbf{n}$	scalar	m/s
$\boldsymbol{\omega}_t$	Relative angular velocity tangent to $\mathbf{n}$	vector	rad/s

Table 2.2: Volumetric normal contact model measured quantities.

Chapter 3

Normal Contact Experiments

3.1 Experiments

The purpose of the experiments is to determine parameters for the volumetric contact model and to validate that model. Parameters to be determined include a volumetric stiffness constant, a hysteretic damping factor, and friction parameters. Of interest for validation are the volume-normal force relationship, bristle-friction model, spinning friction torque model, and the Contensou effect [2]. The experiments have been divided into those pertaining to the normal contact forces and those for the friction forces. In this section, the normal force experiments are described.

For the contact normal force model, measurements of the displacement and forces in the normal direction are required. Two experiments, one static and one dynamic, are used to determine and validate both the volumetric stiffness and damping parameters separately.

Two different contact specimens were designed to be used against a flat plate. The first is spherical, and the results from volumetric contact simulation can be compared directly with those from Hertz theory. The second is cylindrical, with a flat end forming one of the contact surfaces with the opposing plane. This specimen does not satisfy the assumptions in Hertz theory of a small contact patch and non-conforming geometries, which allows testing of the volumetric model in cases where Hertz theory does not apply.

3.1.1 Volumetric stiffness

The specimen is mounted horizontally relative to a vertical contact surface, shown in Figure 3.1. Starting from rest, with the specimen touching the contact surface with no forces between them, the force driving the specimen is gradually increased so that the force sensors are loaded quasi-statically. The rate in displacement was limited to 12 $\mu m/s$, pausing for one second at each programmed position, such that the effect of damping was negligible. Without the effects of damping for the quasi-static case of the volumetric model, the magnitude of force in Equation (2.6) becomes:

$$F_{QS} = k_V V \tag{3.1}$$

The measured displacement was used to find the volume of interference, so that a volumetric stiffness constant, k_V, could be estimated through a linear fit of force to volume measurements. To estimate the value of the stiffness parameter, the following cost function was minimized for k_V:

$$c_{vol} = \sum_k \left[F^k_{meas} - k_V V(\delta^k)\right]^2 \tag{3.2}$$

where F^k_{meas} are the sampled force measurements and $V(\delta^k)$ are estimates of the volume of interference derived from position measurements, δ^k, and dependent on the specimen volume chosen. However, the exact point of contact ($\delta = 0$) is also unknown, since the experiment will begin with the specimen and contact surface separated. Thus, the point of contact, p_0, must be also be estimated from the raw position measurements, p^k,

$$\delta^k = p^k - p_0 \tag{3.3}$$

giving a non-linear optimization problem for minimizing c_{vol} in two parameters, k_V and p_0,

$$c_{vol} = \sum_k \left[F^k_{meas} - k_V V(p^k - p_0)\right]^2 \tag{3.4}$$

For spherical specimens, results can also be compared with Hertz theory. From Equation (1.2) and $n = \frac{3}{2}$, a different cost function can be determined:

$$c_{Hertz} = \sum_k \left[F^k_{meas} - k(\delta^k)^{3/2})\right]^2 \tag{3.5a}$$

$$= \sum_k \left[F^k_{meas} - k(p^k - p_0)^{3/2})\right]^2 \tag{3.5b}$$

giving a nonlinear least-squares minimization problem for k and p_0.

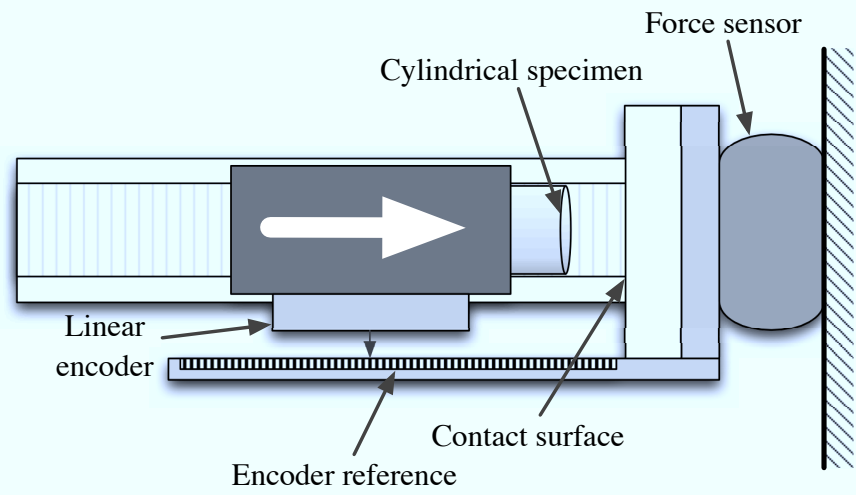

Figure 3.1: Normal force configuration of the experimental apparatus mounted with a cylindrical specimen.

3.1.2 Damping

Equation (2.7) shows that the hysteretic damping factor a in free collision depends on the initial normal velocity at impact, v_n^i, and a kinematic coefficient of restitution, e. With a known volumetric stiffness and measured displacements, velocities, and forces, the damping factor and coefficient of restitution can be estimated.

Many experiments for determining the coefficient of restitution in free collision rely on drop testing. For the purposes of these experiments, very low contact velocities of no more than a few millimetres per second, as might be expected in complex robotic space operations, are desired. In order for collisions to be limited to such velocities, drop heights of less than a micron above the contact surface would be required. It would be extremely difficult to position and measure such an experiment with any reasonable precision accurately.

In the case of these experiments, the specimen is connected to an actuator to regulate the speed of collision. Thus, the experiments do not involve free collision, and the notion of a coefficient of restitution, either kinetic or kinematic, does not apply. Thus, we cannot use Equation (2.7) to determine a.

The specimen is brought into contact with the force plate at different motor-driven

velocities and the subsequent forces and displacements are measured. For each case, the damping factor, a is estimated. A relationship between a and v_n^i will be established, but this relationship cannot be compared back with a coefficient of restitution as with Gonthier [1].

To estimate the hysteretic damping parameter from measured results, the forces measured during quasi-static experiments can be compared with those measured when the specimen is in motion. The force under damping should be given by

$$F_{damped} = F_{QS}(1 + av_{cn}) \tag{3.6}$$

where F_{QS} is the estimated force with no damping from Equation (3.1). To estimate the value of the damping parameter, the following cost function must be minimized:

$$c_{damp} = \sum_k \left(F_{meas}^k - F_{QS}^k(1 + av_{cn}^k)\right)^2 \tag{3.7}$$

where F_{meas}^k are the sampled force measurements and F_{QS}^k are the quasi-static force estimates from the position data, calculated using Equation (3.1). The speeds v_{cn}^k are estimated using a first-order central finite difference approximation of the position data:

$$v_{cn}^k = \frac{d\delta^k}{dt} \approx \frac{\delta^{k+1} - \delta^{k-1}}{t^{k+1} - t^{k-1}} \tag{3.8}$$

3.2 Apparatus

An apparatus has been developed to experimentally validate these models, as shown in Figure 3.2. The apparatus has two configurations, one for validating the normal contact models and the other for the friction models. The normal configuration uses a linear actuator to drive a rigidly mounted specimen into a normal contact surface, which is mounted to a force transducer with a configured resolution of 0.1 N. specimen position relative to the contact surface is measured through a linear encoder with a resolution of up to 1.22 nm. For the friction configuration, the same linear actuator and encoder are employed for translational motion. The friction configuration will be explained later in Chapter 5.

The normal configuration with a cylindrical specimen is depicted in Figure 3.1. A 316 stainless steel specimen is rigidly clamped to the linear actuator. Also rigidly attached to

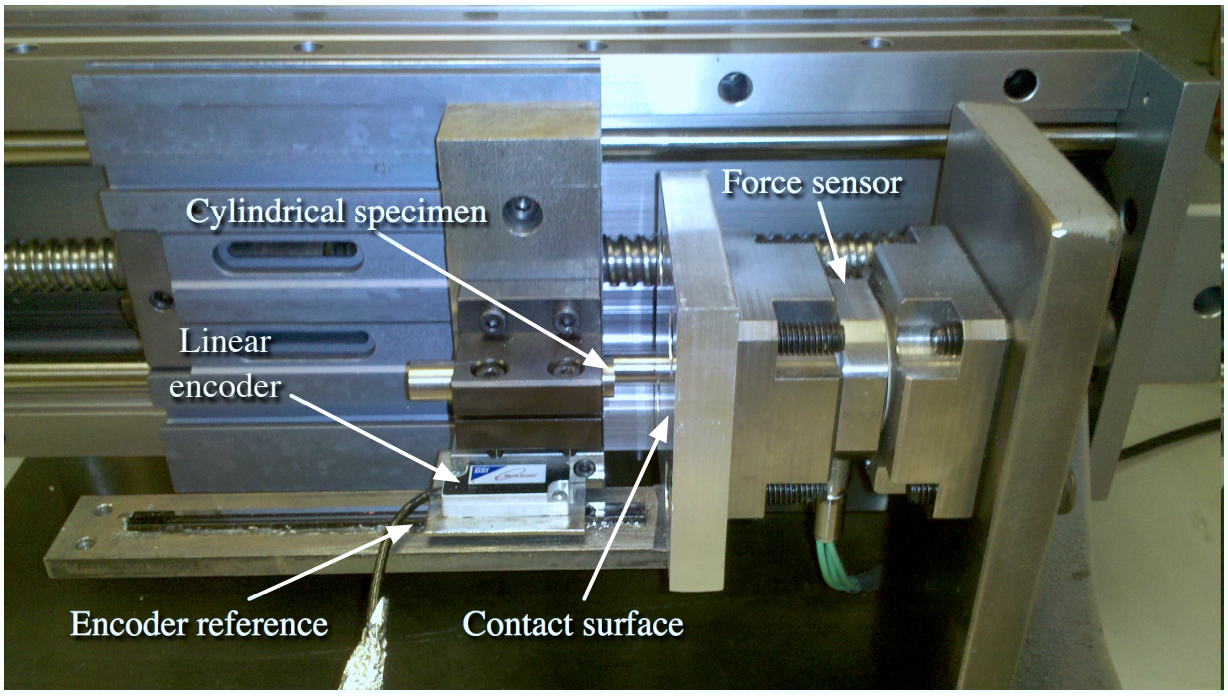

Figure 3.2: Mechanical apparatus for contact experiments, shown in the normal configuration.

the actuator is a linear encoder which measures the position of the specimen relative to a glass reference grating. This reference is mounted to the force sensor.

3.2.1 Contact surfaces

Different deformable contact surfaces can be mounted in front of the piezoelectric force sensor. Metal contact surfaces were employed, an aluminum plate and an AZ31 magnesium alloy. The aluminum (6061) plate was 25.4 mm thick and polished to 1200 grit. The AZ31 magnesium alloy was 22 mm thick and loaded perpendicular to the extruded direction. The magnesium surface was polished to 1500 grit, but quickly dulled due to oxidation.

The magnesium alloy was found to have a higher modulus of elasticity in the extruded direction than the transverse directions, meaning the material is anisotropic. Experimental results for point contact with this material may not follow Hertz law, as the theory assumes isotropy [18].

These materials are more compliant than the specimen, so it is assumed that the majority of the deformation will take place in the contact surface rather than the specimen. Using Young's Modulus (listed in Table 3.1) for each material as a rough measure of relative stiffness, it is estimated that the specimen will account for approximately one-fourth of the compliance when applied to aluminum and one-sixth with magnesium AZ31. However, we can still use Equation (2.6) for the normal force, since it retains the same form if both bodies are deformable [1].

Material	Modulus of Elasticity $E\ (GPa)$	Possion's Ratio ν
Magnesium	$35 - 40$	0.35
Aluminum	69	0.33
316 stainless steel	200	0.27

Table 3.1: Elastic properties for contact surface and specimen materials [24].

3.2.2 Specimen geometries

Both a spherical and a flat cylindrical specimen were employed. The two contact specimens were constructed from 316 stainless steel.

Spherical specimen

The spherical specimen has the advantage of being largely indifferent to alignment due to its shape, having a sphericity of 2.5 μm over a diameter of 19.05 mm. Results from the validation can also be compared with those of Hertz theory for sphere-on-plane contact. The Hertzian contact force is given by Equation (1.2). A theoretical value for Hertzian stiffness, k, can be determined by [18]:

$$k = \frac{4}{3} E^* r^{1/2} \tag{3.9}$$

where r is the radius of the sphere, which in this case was 9.52 mm. E^* is defined by the elastic properties of the materials:

$$\frac{1}{E^*} = \frac{1 - \nu_i^2}{E_i} + \frac{1 - \nu_j^2}{E_j} \tag{3.10}$$

where E_i and E_j are the elastic moduli and ν_i and ν_j are the Poisson's ratios of the bodies, found in Table 3.1.

For the volumetric model, the volume of interference between a sphere and a plane is a spherical cap, assuming that the midpoint of the sphere does not surpass the boundary of the plane. The magnitude of this volume can also be expressed in terms of depth of penetration, δ [25]:

$$V = \frac{\pi}{3} \delta^2 (3r - \delta) \tag{3.11}$$

where r is the radius of the sphere.

Cylindrical specimen

For the second specimen, a cylinder was selected because it provided a relatively large conforming contact surface that would demonstrate the usefulness of the model in cases where point contact could not be assumed. Also, because contact pressure is spread over a

larger surface area than with sphere-on-sphere or sphere-on-plane, there is less risk of plastic deformation from a highly concentrated point load. Finally, assuming the specimen and the contact surface are perfectly aligned, the volume of interference between the cylinder and the plane can easily be expressed in terms of the depth of penetration, δ:

$$V = \pi r^2 \delta \tag{3.12}$$

where r is the radius of the cylinder, which is 5 mm in this case. Thus, the volume of interference and consequently, the normal force in the model, have a linear relationship with the displacement. In the quasi-static case,

$$f_N = k_V \pi r^2 \delta \tag{3.13}$$

In this specific perpendicular case, the quantity $k_V \pi r^2$ could be reduced to a single constant, however for these experiments, k_V is retained as separate constant to remain consistent with the general volumetric model.

While Hertz point contact models cannot be used for a flat cylinder in contact with a plane, other classical solutions exist. Sneddon [26] determined the relation between force and displacement for a rigid cylindrical punch on an elastic half-space:

$$f_N = 2 r E^* \delta \tag{3.14}$$

where r is the radius of the cylindrical punch and E^* is defined by the elastic properties of the half space:

$$E^* = \frac{E}{1 - \nu^2} \tag{3.15}$$

where E and ν are the elastic modulus and Poisson's ratio, respectively. In the case where the punch is also compliant (as it is in the case of these experiments), we can use Equation (3.10) to find E^* in terms of the properties of both bodies.

When Equations (3.13) and (3.14) are compared, we note that both models are linear in terms of δ. From these equations, a theoretical value for the volumetric stiffness can also be determined:

$$k_V = \frac{2E^*}{\pi r} \tag{3.16}$$

Experimental results can be compared with this theoretical value. In this case, k_V is dependent on the radius of the specimen. This suggests that volumetric stiffness may not be invariant with respect to geometry, but may have an inverse relationship with the size of the contact patch.

3.3 Results and Discussion

3.3.1 Volumetric stiffness

Spherical specimen

The spherical specimen was applied to each of the contact surfaces with up to 20 N of force. Using non-linear optimization, contact points and stiffness parameters were determined for both the Hertzian and volumetric models. Stiffness values are presented in Table 3.2 and measured values and model fits are shown in Figures 3.3 and 3.4. Measured Hertzian contact stiffnesses were about 2/3 of theoretical values determined using Equation (3.9) for both contact surfaces. Note that in the figures, the zero point along the horizontal axis does not correspond to the point of contact, but to the relative position with respect to the initial position of the experiment. Contact points are found by fitting the model to the data.

Material	Experimental Hertzian stiffness ($\frac{N}{m^{1.5}}$)	Theoretical Hertzian stiffness ($\frac{N}{m^{1.5}}$)	Volumetric stiffness ($\frac{N}{m^3}$)
Magnesium	3.02×10^9	4.66×10^9	3.82×10^{13}
Aluminum	4.79×10^9	7.34×10^9	7.59×10^{13}

Table 3.2: Hertzian and volumetric stiffnesses for spherical specimen.

Both models provide good fits of the measured forces and displacements. For the aluminum, the Hertzian model provides a closer fit of the data compared with the volumetric model, with root mean square values of 0.158 and 0.221, respectively. For the magnesium, the volumetric model provides a closer fit with a root mean square error of 0.645 compared with 0.837 for the Hertzian model. However, it should be recalled that the magnesium alloy is orthotropic, so the surface cannot be expected to behave according to Hertz law, as predicted earlier.

Figure 3.3 and Fig. 3.4 show that the estimated contact point is different for the volumetric and Hertzian models. For the metals, this difference is less than half a micron, which should not significantly impact the simulation of larger robotic tasks. The expressions for

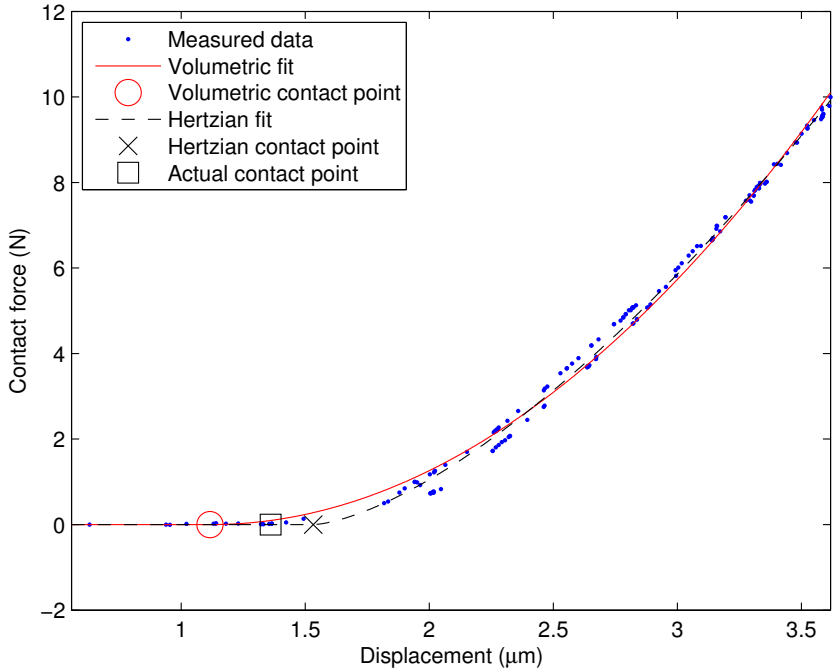

Figure 3.3: Quasi-static force versus displacement for spherical contact on aluminum.

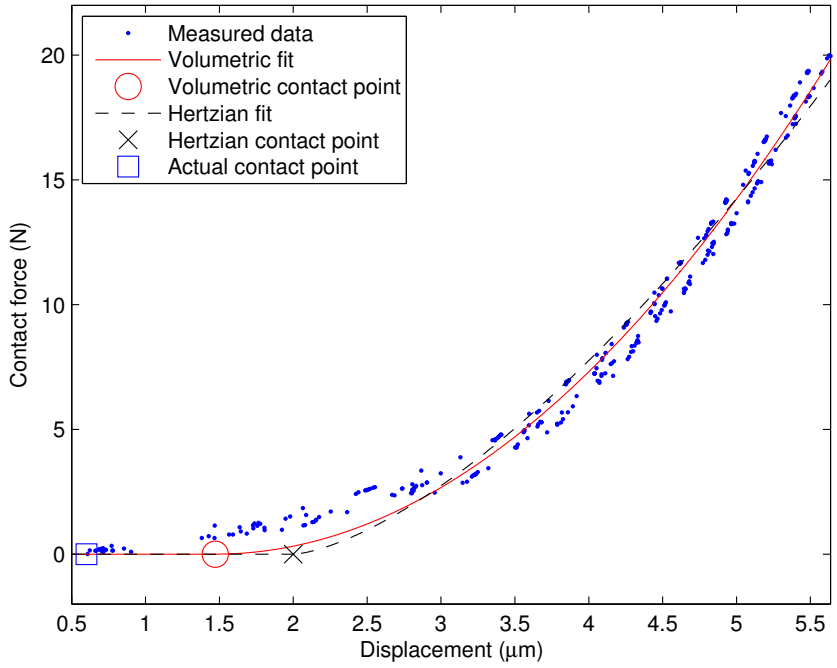

Figure 3.4: Quasi-static force versus displacement for spherical contact on magnesium alloy.

force have different orders with respect to displacement around the point of contact for the models. Using 'Big O' notation for the Hertzian model,

$$F = O(\delta^{1.5}) \text{ as } \delta \to 0 \tag{3.17}$$

and for the volumetric model,

$$F = O(\delta^{2}) \text{ as } \delta \to 0 \tag{3.18}$$

Thus, near the contact point, the estimated force will rise more rapidly for the Hertzian model than for the volumetric model.[1] Since the force-displacement slope for the volumetric profile is numerically shallower, the nonlinear least squares fitting operation will tend to estimate the contact point occurring for the volumetric model slightly ahead of the Hertzian model.

Another feature of this difference in order between the two models is the impact these will have on the magnitude of the stiffness parameters estimated. For example, let us assume that according to classical elastic theory, the Hertz model accurately describes the relationship between force and displacement. If the force range applied were to be extended, to say 100 N, the estimated volumetric stiffness would be less than for a maximum force of 20 N, as the volumetric model has a higher order than Hertz law for low values of δ. Thus, the volumetric stiffness determined is more dependent on the range of forces being measured.

The 'actual' measured point of contact, (based on where contact forces are first detected), differs from points of contact estimated from non-linear optimization with the magnesium sample (Figure 3.4). There is an initial region of lower slope for the first few microns in the force-displacement curve that is not accounted for in either model. However, it should be recalled that the magnesium alloy is anisotropic, so the surface cannot be expected to behave according to Hertz law, as predicted earlier.

The initial contact region for magnesium may be accounted for by the asperities of the contact surface. The surface of the magnesium sample was smoothed to a reflective 1500 grit, or 3 μm, but rapidly became dull. These surface asperities reduce the surface area of

[1]It should be noted that if k_V is not assumed to be constant, but varies with the size of the contact patch as predicted by Equation (3.16) in the cylindrical case in Section 3.2.2, the two models may in fact share the same order in δ. If the volumetric stiffness is inversely related to the radius of the contact area, $\sqrt{2r\delta}$ in this case, both the Hertzian and volumetric models share the same order.

the contact patch, leading to a much lower force-displacement slope until these asperities have been flattened. In addition, the elastic properties of the oxidized magnesium surface is unknown, and may account for this initial difference.

A small amount of hysteresis is observed in the measurements for both materials, such that there is slightly less contact force when the specimen is being reversed as compared to when it is applied. Since the specimen is allowed to rest after reaching each servo encoder count, this hysteresis cannot be attributed to damping forces in the model. The amount of hysteresis will increase with higher maximum loads, suggesting some small amount of permanent deformation is taking place. There was no visible damage to the surface.

Cylindrical specimen

Measurements using a cylindrical specimen are shown in Figures 3.5 and 3.6. Attempts at a linear fit of the data are shown as a solid line, labelled 'Perpendicular fit.' The results do not conform well to a linear fit, which the volumetric model would call for. Classical elastic theory would also suggest a linear fit between displacement and force for a perpendicular cylinder on a plane. This suggests that there are non-negligible surface asperities on the cylindrical specimen, or that the surfaces are misaligned. Additionally, estimated stiffness values (Table 3.3) are two orders of magnitude less than theoretical predicted in Equation (3.16).

Material	Experimental volumetric stiffness ($\frac{N}{m^3}$)	Theoretical volumetric stiffness ($\frac{N}{m^3}$)
Magnesium	7.88×10^{10}	5.17×10^{12}
Aluminum	1.24×10^{11}	8.82×10^{12}

Table 3.3: Volumetric stiffnesses for the cylindrical specimen.

Sources of misalignment in the experiment may include the mounting of the specimen to the ball screw (along the horizontal axis in the plane of the contact surface), and the relative alignments of the ball screw and the force sensor (along the vertical axis).

For the purpose of modelling the contact in the misaligned case, it is assumed that angle from the normal, γ, (shown in Figure 3.7) does not change significantly over the the loading

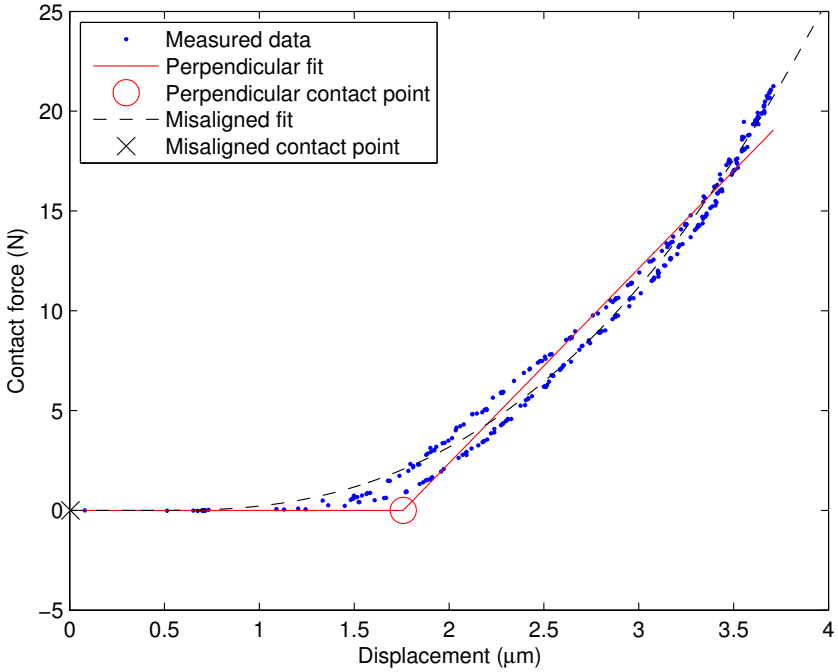

Figure 3.5: Quasi-static force versus displacement for cylindrical contact on aluminum.

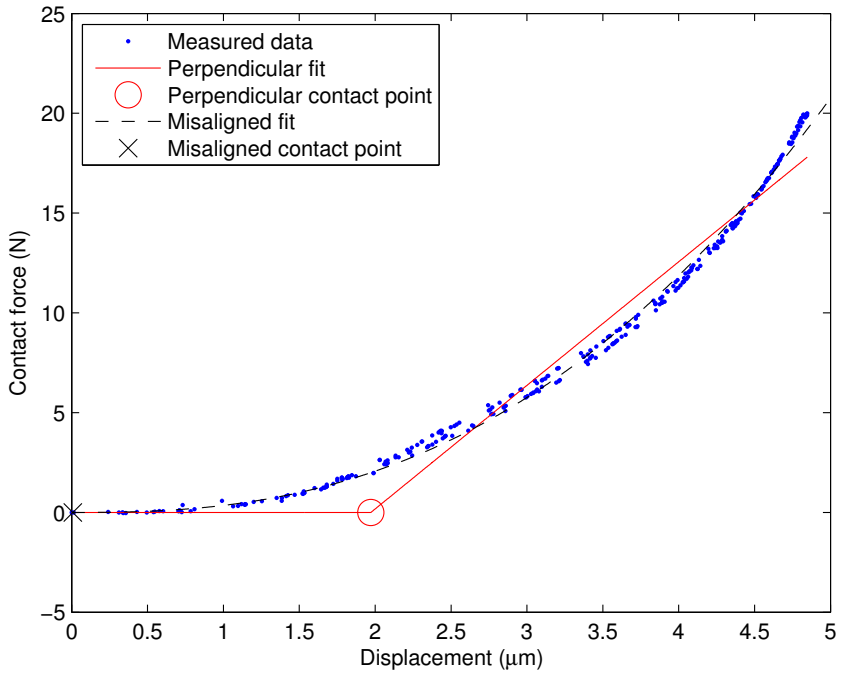

Figure 3.6: Quasi-static force verus displacement for cylindrical contact on magnesium alloy.

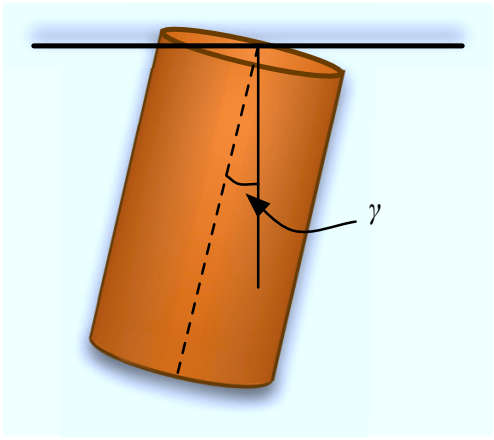

Figure 3.7: Misaligned cylindrical specimen, with deviation $\gamma$from the normal.

and unloading sequence. Unfortunately, no analytical solution exists in classical contact theory for the relationship between force and displacement for an inclined cylinder on a plane with incomplete contact [27]. For the volumetric model, the volume of a cylindrical wedge [25] can be used to estimate volume of interference:

$$V = \frac{\delta r^3}{3b}\left[2\sin\phi - \cos\phi\left(3\phi - \frac{1}{2}\sin 2\phi\right)\right] \tag{3.19}$$

where δ, b, and ϕ are shown in Figure 3.8. Wedge length b is given by

$$b = \frac{\delta}{\tan\gamma} \tag{3.20}$$

while ϕ can be determined by

$$\phi = \cos^{-1}\left(\frac{r-b}{r}\right) \tag{3.21}$$

Substituting these into (3.19) gives a formula for volume solely in terms of r, δ, and γ. In terms of parameter identification from the experimental results, this volume model requires an additional angle misalignment term in addition to the volumetric stiffness and contact boundary unknowns for the perpendicular case.

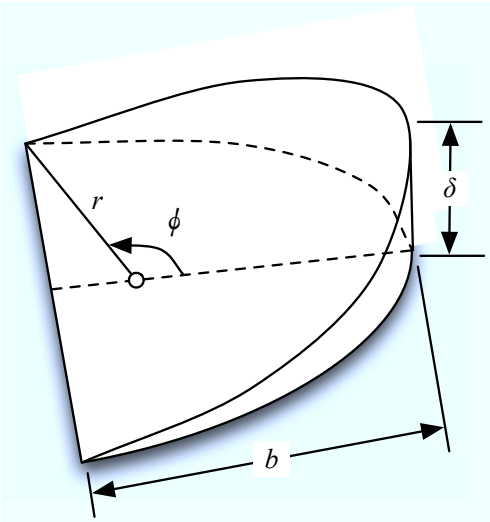

Figure 3.8: Cylindrical wedge.

The stiffness parameter can be treated as known by substituting the values determined from the theoretical estimates for perpendicular contact in Table 3.3, which were calculated

using Equation (3.16). Non-linear optimization of c_{vol} in Equation (3.4) was used to find unknowns p_0 and γ with the 'Trust-Region' method of the *MATLAB Curve-Fitting Toolbox*. The resulting displacement-force curves for the aluminum and magnesium surfaces are shown as dashed lines in Figures 3.5 and 3.6. This off-normal model agrees well with the experiments. The estimated off-normal angles were determined to be 0.46° and 0.32° for the magnesium and aluminum, respectively. In both cases, the misalignment is less than half a degree.

Misalignments of this small a magnitude would be very difficult to perceive visually. However, it is also possible that the machined specimen has non-negligible surface asperities.

3.3.2 Damping

Experiment execution and processing

As spherical specimens offered results in quasi-static testing that agreed well with the model, spherical specimens were employed for the dynamic tests. The hard metallic contact surfaces were impacted at speeds ranging from 0.1 to 1 mm/s. The motor controller was programmed to track the desired velocity using the signal from the internal encoder of the servo. The servo encoder, when connected to the ball screw system, had a resolution of 1.25 μm per encoder count. With a frequency of 16 kHz, the LabVIEW controller was observed to maintain the desired velocity to within about 0.1 mm/s, due to the small number of servo encoder counts between time intervals.

Measurements of force and position commenced prior to contact, with a sampling frequency of 1 kHz. Accurate measurements of the position of the specimen came from the high resolution linear encoder. Once contact had occurred, the motor would continue to attempt to track the desired velocity. Due to the compliance in the ball screw system and the apparatus, the actual velocity of the specimen itself relative to the contact surface slowed down, even though the speed of the motor was maintained.

Control and data collection loops were executed on separate processes in the real-time system. The control loop (which provided commands to the motion controller, operating at a much higher frequency), operated at a frequency of 10 Hz, and the data loop operated at 1 Hz, loading 1000 force and position samples at a time from the capture cards into

memory. The control loop would monitor the latest force measurements in memory to determine if contact had occurred, at which point it would instruct the motor to stop and reverse and toggle a flag that would instruct the data collection loop to stop. Thus, at least a second worth of sample data following contact would be collected.

A subset of the sampled data was then selected for comparison with the model with the following methodology. For each collision, the position contact where contact first occurred was estimated from the force data. The preprocessor then selects 0.1 s of data, beginning at a point 2 servo encoder counts (2.5 μm) prior to contact. An example of such a sample is shown in Figure 3.9.

With the position data, the volume of interference can be determined, allowing the contact force without damping effects to be estimated for each sampled position. Volumetric stiffness values determined with the spherical specimen in Section 3.3.1 are used. These estimated force values in the case of Figure 3.9 are shown as a dashed line in the lower force graph. It is observed that these estimates are lower than the sampled force values, indicating that damping has occurred.

The final force estimated using position data, with damping included, is shown in Figure 3.9 as a solid line. The line appears noisy due to the poor speed estimates. At very low speeds, there is only a small number of encoder counts between sample intervals. The effect of the error in speed estimates on the magnitude of the estimated force is increased as the penetration depth increases. Nevertheless, the agreement between the model and experiments is still quite good.

Measured damping factors

Measured values of the hysteretic damping factor for the magnesium alloy and aluminum are shown in Figures 3.10 and 3.11, respectively. It is observed that the damping factor can be inversely related to the initial impact velocity as predicted in Equation (2.7). A least-squares fit of an inverse relation shown in the figures as a solid line.

Since the impact is driven and not free collision, the notion of a coefficient of restitution does not apply. However, the inverse relationship between the hysteretic damping factor a and the impact velocity observed is similar to Equation (2.7), as long as the coefficient of restitution e is assumed to be constant with respect to v_{cn}^{i}. This coefficient e was found to be 0.134 for aluminum and 0.114 for magnesium.

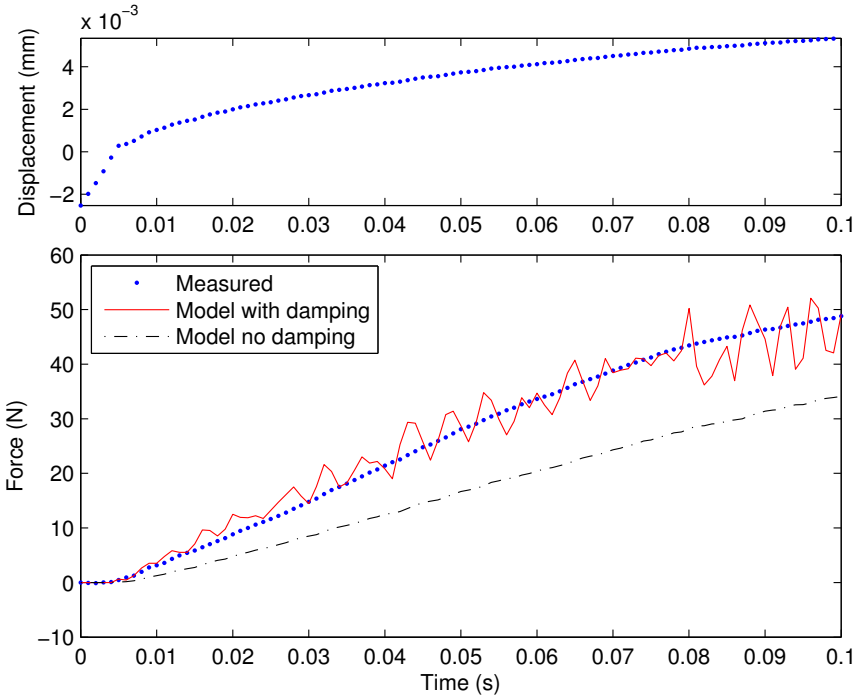

Figure 3.9: Force and displacement measurements with static and dynamic models for impact at 0.58 mm/s on magnesium alloy.

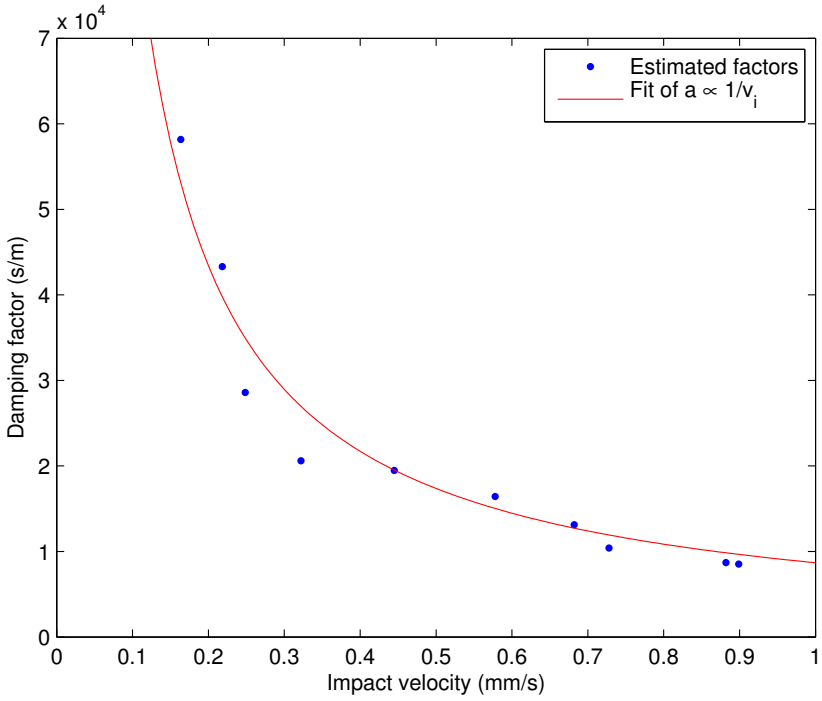

Figure 3.10: Estimated hysteretic damping factors from experimental results for magnesium versus impact velocity.

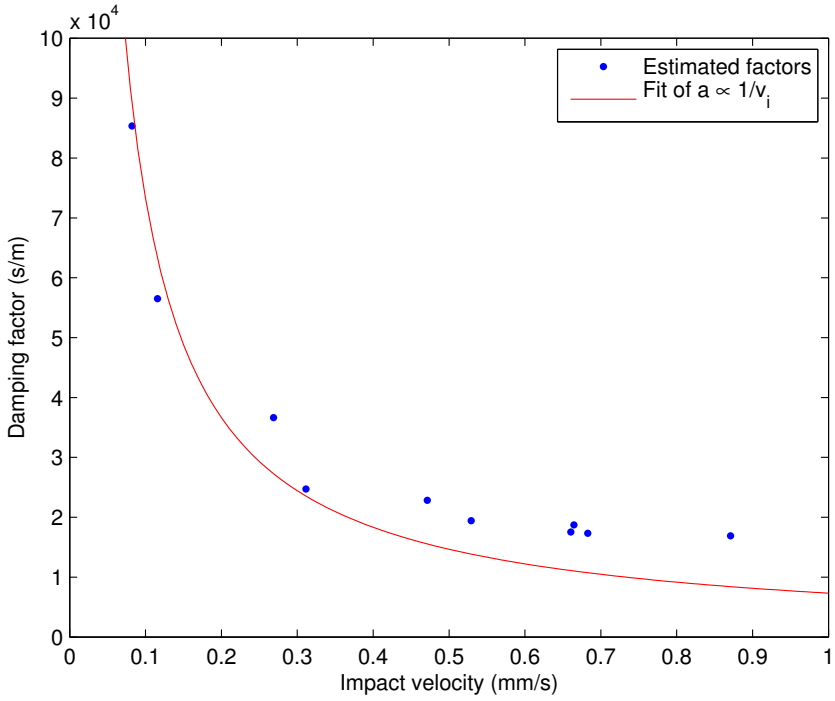

Figure 3.11: Estimated hysteretic damping factors from experimental for aluminium results versus impact velocity.

3.3.3 Sources of error

Alignment

As discussed in the cylindrical specimen results, it possible that the apparatus is not well aligned. In the spherical specimen case, this minor misalignment should have negligible impact on results. However, in the case of the cylindrical specimen, even small misalignments may result in incomplete contact over the course of the experiment.

Surface roughness

Surface asperities can result in incomplete contact [28] and have been shown to be a significant factor in the reduction of contact stiffness, both theoretically and experimentally [22]. This leads to lower than predicted contact stiffnesses, as there is less material being compressed after initial contact. In terms of the volumetric model, this means there is an unknown volume of interference that would be less than that for ideal geometries, and depends on the surface roughness.

The aluminum surface was polished with 1200 grit sandpaper, while the magnesium was polished with 1500 grit sandpaper. These surfaces should have surface asperities no greater than 5 μm and 3 μm, respectively. Note that the magnesium dulled quickly after polishing (as expected). It is not known what impact this oxidation had on the properties of the magnesium surface.

The spherical specimen was constructed from a stainless steel ball-bearing with a sphericity of 2.5 μm. The cylindrical specimen was specified to have a surface roughness of 0.8 μm.

Linear encoder distortion

Compliance in the apparatus under higher loads would cause the linear encoder to deflect away from the encoder reference. This deflection created a distortion in the position measurements that grew with increased pressure. Forces in the quasi-static experiments were limited to 20 N so that deflection of the position equipment was negligible.

Other compliances

The apparatus was designed such that the displacement measurements would capture primarily the strain within the contacting materials. Thus, the position encoder was placed in proximity to the specimen mounting hardware and the reference was mounted directly behind the contact surface. However, there is the possibility of some compliance within the specimen mounting bracket and the bolts holding it in place. These compliances would serve to decrease the magnitude of the stiffness parameters estimated, and could in part explain why estimated Hertzian stiffnesses were less than theoretical values.

Dynamic response of the force sensor

It was important that the dynamic behaviour of the force transducer not affect the measurements during the dynamic experiments. The resonant frequencies of the transducer with the contact surfaces mounted were determined to be 4.08 kHz for aluminum and 4.46 kHz for magnesium. The force transducer will act to attenuate oscillations above these frequencies. The experiments used a sampling frequency of 1 kHz, which is below the dynamic response for either material.

Sensor noise and drift

Measurements from piezoelectric force transducer at constant load were observed to have a standard deviation of 0.085 N. The specified repeatability of the charge amplifiers was 0.1 N. This represents 0.5% of the force range measured during the quasi-static experiments and 0.1% during the dynamic experiments.

The force transducer and charge amplifier were determined to have a drift of up to 0.1 N/s after about an hour of warm-up. This drift was determined to remain consistent over several minutes. In order to compensate for this drift, the force measured at the end of the experiment, when the specimen was withdrawn, was used to determine the average drift. The modelled drift was then subtracted from the force measurements.

Chapter 4

Volumetric Friction Model

4.1 Introduction

Gonthier proposes a seven-parameter friction model to be used in conjunction with the volumetric normal contact model [1]. This chapter outlines the elements of this model that will be tested in Chapter 5.

Section 4.2 describes a general framework for friction forces and torques, as well as concepts of average surface velocity and sticking state [2]. A bristle friction model, developed for point contact models [5] and extended to spinning friction torque [1], is described in Section 4.3. Section 4.4 and Section 4.5 cover the inclusion of dwell-time dependency [5] and the Contensou effect [2, 1], respectively.

4.2 Basic Friction Model Framework

4.2.1 Forces

For point contact models, friction is often modelled with Equation (1.6), where the friction coefficient μ depends on the nature of the motion of the bodies at the point of contact. The friction force generally resists motion, so a vector expression for friction force can be of the form

$$\mathbf{f}_t = -\mu f_n \frac{\mathbf{v}_t}{|\mathbf{v}_t|} \tag{4.1}$$

where $\mathbf{v}_t$ is the relative velocity between the bodies at the point of contact, and μ in this case is a friction coefficient dependent on the model implementation.

In the volumetric normal contact model described in Chapter 2, contact takes place over a surface within the volume of interference, rather than at a single point. Gonthier et al. [2] considered the infinitesimal friction element $d\mathbf{f}_t$:

$$d\mathbf{f}_t = -\mu \frac{\mathbf{v}_t}{|\mathbf{v}_t|} df_n \tag{4.2}$$

Integrating over the contact surface yields

$$\mathbf{f}_t = -\mu f_n \frac{\mathbf{v}_{sct}}{|\mathbf{v}_{sct}|} \tag{4.3}$$

where $\mathbf{v}_{sct}$ is the relative velocity between the bodies in contact at the centroid of the contact surface $\mathbf{s}_c$, tangent to the contact surface S.

Further, since friction can take place over an area, the relative velocity between the bodies may not be uniform over all points along the surface, leading to a friction torque. This torque acts to resist the relative angular motion of the bodies and is known as the spinning friction torque. The infinitesimal torque $d\boldsymbol{\tau}_s$ is

$$d\boldsymbol{\tau}_s = -\boldsymbol{\rho}_s \times d\mathbf{f}_t \tag{4.4}$$

which when integrated becomes

$$\boldsymbol{\tau}_s = -\frac{\mu f_n}{V} \mathbf{J}_s \cdot \frac{\boldsymbol{\omega}_n}{|\boldsymbol{\omega}_n|} \tag{4.5}$$

where $\boldsymbol{\omega}_n$ is the relative angular velocity about $\mathbf{n}$ at the contact centroid. As with the normal model, the surface inertial tensor $\mathbf{J}_s$ can be closely approximated with the volume inertia tensor $\mathbf{J}_V$.

It can be shown that

$$\mathbf{n} \cdot \mathbf{J}_s \cdot \mathbf{n} = \mathbf{n} \cdot \mathbf{J}_V \cdot \mathbf{n} = r_{gyr}^2 V \tag{4.6}$$

where r_{gyr} is the radius of gyration of the volume about the normal. This allows us to rewrite Equation (4.5) as

$$\boldsymbol{\tau}_s = -\mu r_{gyr}^2 f_n \frac{\boldsymbol{\omega}_n}{|\boldsymbol{\omega}_n|} \tag{4.7}$$

4.2.2 Stick-slip state and average surface velocity

Whether two bodies in contact are sticking or slipping is determined by the rate of tangential motion between the surfaces of the bodies. The average surface velocity v_{avg} is defined by the average relative tangential velocity of all points on the contact surface, and can be expressed in terms of translational and angular speeds, $\mathbf{v}_{sct}$ and $\boldsymbol{\omega}_n$:

$$\begin{aligned} v_{avg}^2 &= \mathbf{v}_{sct} \cdot \mathbf{v}_{sct} + \boldsymbol{\omega}_n \cdot \frac{\mathbf{J}_s}{V} \cdot \boldsymbol{\omega}_n \\ &= \mathbf{v}_{sct} \cdot \mathbf{v}_{sct} + (r_{gyr}|\boldsymbol{\omega}_n|)^2 \end{aligned} \tag{4.8}$$

A function s is used to determine the 'sticking state', that is, the degree to which the bodies are either sticking or sliding across each other.

$$s = e^{-\frac{v_{avg}^2}{v_s^2}} \tag{4.9}$$

where v_s is the velocity where the Stribeck effect occurs, that is, transition between sticking and slipping. When $s \approx 1$, the bodies are not moving tangentially relative to each other, but when $s \approx 0$, the bodies are slipping freely. Intermediate values between 0 and 1 indicate that friction is transitioning between sticking and slipping. Slipping will occur if the bodies are translating or rotating relative to each other.

4.3 Bristle Model

4.3.1 Translational friction force

As with the point contact friction model described by Gonthier et al. [5], the volumetric friction model assumes that the surface asperities of the bodies in contact act as flexible 'bristles' that push against and rub past each other. The amount of deformation is modelled as $\mathbf{z}_{sc}$, a vector along the contact surface called the bristle state. For the volumetric model, this deformation is measured from the centroid of the contact surface, $\mathbf{s}_c$. The friction force acts to oppose the deformation of the bristles:

$$\mathbf{f}_{br} = -f_n(\sigma_0 \mathbf{z}_{sc} + \sigma_1 \dot{\mathbf{z}}_{sc}) \tag{4.10}$$

where σ_0 is the bristle stiffness, and σ_1 is the bristle damping.

The bristle deformation rate $\dot{\mathbf{z}}_{sc}$ is further divided into two sub-models for sticking and slipping, $\dot{\mathbf{z}}_{st}$ and $\dot{\mathbf{z}}_{sl}$ respectively. The sticking state s is used to determine the effect of each on the overall deformation rate

$$\dot{\mathbf{z}}_{sc} = s\dot{\mathbf{z}}_{st} + (1-s)\dot{\mathbf{z}}_{sl} \tag{4.11}$$

During the sticking phase, the bristles deform at the same rate as the bodies translate relative to each other,

$$\dot{\mathbf{z}}_{st} = \mathbf{v}_{sct} \tag{4.12}$$

While slipping, a Coulomb friction model is assumed:

$$\mathbf{f}_c = -\mu_d f_n \mathrm{dir}(\mathbf{v}_{sct}) \tag{4.13}$$

where μ_d is the kinetic friction coefficient, and $\mathrm{dir}(\mathbf{v}_{sct})$ is a function that gives a unit vector in the direction of $\mathbf{v}_{sct}$. Gonthier assumes that $\dot{\mathbf{z}}_{sc} \approx \dot{\mathbf{z}}_{sl}$ and combines Equation (4.10) with Equation (4.13) to yield

$$\dot{\mathbf{z}}_{sl} = \frac{\mu_d}{\sigma_1}\mathrm{dir}(\mathbf{v}_{sct}) - \frac{\sigma_0}{\sigma_1}\mathbf{z}_{sc} \tag{4.14}$$

Combining Equation (4.12) and Equation (4.14) into Equation (4.11) gives

$$\dot{\mathbf{z}}_{sc} = s\mathbf{v}_{sct} + (1-s)\left(\frac{\mu_d}{\sigma_1}\mathrm{dir}(\mathbf{v}_{sct}) - \frac{\sigma_0}{\sigma_1}\mathbf{z}_{sc}\right) \tag{4.15}$$

The friction force f_t is limited by the maximum friction coefficient μ_{max}

$$f_t \leq \mu_{max} f_n \tag{4.16}$$

The friction coefficient is determined by the sticking state:

$$\mu_{max} = \mu_d + s(\mu_s - \mu_d) \tag{4.17}$$

where μ_s is the maximum static (i.e. sticking) friction coefficient. In order to bound the magnitude of the friction force, Gonthier defines a saturation function

$$\mathrm{sat}(\mathbf{u}, u_{max}) = \begin{cases} \mathbf{u} & ; \quad |\mathbf{u}| \leq u_{max} \\ \frac{\mathbf{u}}{|\mathbf{u}|}u_{max} & ; \quad |\mathbf{u}| > u_{max} \end{cases} \tag{4.18}$$

allowing $\mathbf{f}_t$ to be expressed as

$$\mathbf{f}_t = \text{sat}(\mathbf{f}_{br}, \mu_{max} f_n) \tag{4.19}$$

Adding a term proportional to relative tangential velocity for viscous friction, Gonthier finds a combined expression for $\mathbf{f}_t$:

$$\mathbf{f}_t = -f_n[\text{sat}(\sigma_0 \mathbf{z}_{sc} + \sigma_1 \dot{\mathbf{z}}_{sc}, \mu_{max}) + \sigma_2 \mathbf{v}_{sct}] \tag{4.20}$$

where σ_2 is the viscous damping coefficient.

As the friction force is bounded, the bristle deformation rate is also bounded [1]:

$$\dot{\mathbf{z}} = \frac{1}{\sigma_1}\text{sat}(\sigma_0 \mathbf{z}_{sc} + \sigma_1 \dot{\mathbf{z}}_{sc}, \mu_{max}) - \frac{\sigma_0}{\sigma_1}\mathbf{z}_{sc} \tag{4.21}$$

4.3.2 Spinning friction torque

This subsection only considers the case where the bodies are rotating in the normal direction relative to each other, but not moving tangentially. Combined translation and rotation are discussed in Section 4.5.

If two bodies in contact are spinning relative to each other in a direction normal to the contact surface, then not all bristles across the surface deform in the same direction. Gonthier [1] observes that during the sticking phase, the local bristle deformation rate $\dot{\mathbf{z}}$ moves according to the relative body motion at $\mathbf{s}_c$, and thus, the relative local deformation $\mathbf{z}$ is shown to be

$$\mathbf{z} = \mathbf{z}_{sc} + \theta_n \mathbf{n} \times \boldsymbol{\rho}_t \tag{4.22}$$

where θ_n is the relative angular displacement of the bristles about the normal and $\boldsymbol{\rho}_t$ is a vector from $\mathbf{s}_c$ to the point on the contact surface.

With a local bristle deformation, the infinitesimal bristle friction element can be considered,

$$d\mathbf{f}_{br} = df_n(\sigma_0 \mathbf{z} + \sigma_1 \dot{\mathbf{z}}) = \sigma_0 \mathbf{z} df_n + \sigma_1 \dot{\mathbf{z}} df_n \tag{4.23}$$

giving an infinitesimal torque element about $\mathbf{s}_c$ of

$$d\boldsymbol{\tau}_{br} = \boldsymbol{\rho}_s \times d\mathbf{f}_{br} \tag{4.24}$$

Integrating over the contact surface gives

$$\boldsymbol{\tau}_{br} = -r_{gyr}^2 f_n(\sigma_0\theta_n + \sigma_1\dot{\theta}_n)\mathbf{n} \tag{4.25}$$

which allows us to use θ_n as an angular bristle state. Gonthier derives the angular bristle state dynamics similar to the tangential dynamics of Equation (4.15),

$$\dot{\theta}_n = s\omega_n + (1-s)\left(\frac{\mu_d}{\sigma_1 r_{gyr}}\text{sgn}(\omega_n) - \frac{\sigma_0}{\sigma_1}\theta_n\right) \tag{4.26}$$

with a saturation of

$$\dot{\theta_n} = \frac{1}{\sigma_1}\text{sat}\left(\sigma_0\theta_n + \sigma_1\dot{\theta}_n, \frac{\mu_{max}}{r_{gyr}}\right) - \frac{\sigma_0}{\sigma_1}\theta_n \tag{4.27}$$

The spinning bristle torque can then be computed as

$$\boldsymbol{\tau}_s = -r_{gyr}^2 f_n\left[\text{sat}\left(\sigma_0\theta_n + \sigma_1\dot{\theta}_n, \frac{\mu_{max}}{r_{gyr}}\right) + \sigma_2\omega_n\right]\mathbf{n} \tag{4.28}$$

4.4 Dwell-Time Dependency

It has been observed that static friction increases the longer the two objects in contact have been at rest [13]. It is possible that the asperities between the two surfaces begin to adhere to each other over time, requiring that these bonds be broken before sliding may resume. Gonthier et al. attempts to model this effect by including a dwell-time dependency [5].

A second sticking state s_{dw} is introduced to include the influence of how long the bodies have been at rest. This state follows the original sticking state s as follows:

$$s_{dw} = \begin{cases} \frac{1}{\tau_{dw}}(s - s_{dw}) & ; \quad s - s_{dw} \geq 0 \\ \frac{1}{\tau_{br}}(s - s_{dw}) & ; \quad s - s_{dw} < 0 \end{cases} \tag{4.29}$$

where τ_{dw} is a dwell-time dynamics time constant and τ_{br} is the bristle dynamics time constant, that is, σ_1/σ_0. Thus, when the bodies come to rest, s_{dw} will gradually approach 1, but quickly go to zero when the bodies begin moving again.

Equation (4.17) is replaced to include the dwell-dependent sticking state:

$$\mu_{max} = \mu_d + s_{dw}(\mu_s - \mu_d) \tag{4.30}$$

4.5 The Contensou Effect

The force, torque, and bristle state models in Section 4.3 are presented with the assumption that the bodies are moving either tangentially or rotationally, but not both. However, it is known that tangential motion impacts friction torque and rotational motion impacts tangential friction force.

Contensou discovered that tangential sliding friction diminishes as spinning speed increases [17]. This effect is most observable in a spinning floor polisher; it is difficult to push when the machine is turned off, but when the polisher is spinning against the ground, it glides easily. A circular contact surface of radius r is shown in Figure 4.1 undergoing both rotation and translation. The diagram on the left side shows that when the product of angular speed and the radius, $\omega_n r$ is much greater than the tangential velocity v_c, the angular motion dominates the trajectories of the edge points A and B. In this case, the resistance to motion from friction on the surface will 'cancel out' in the tangential direction.

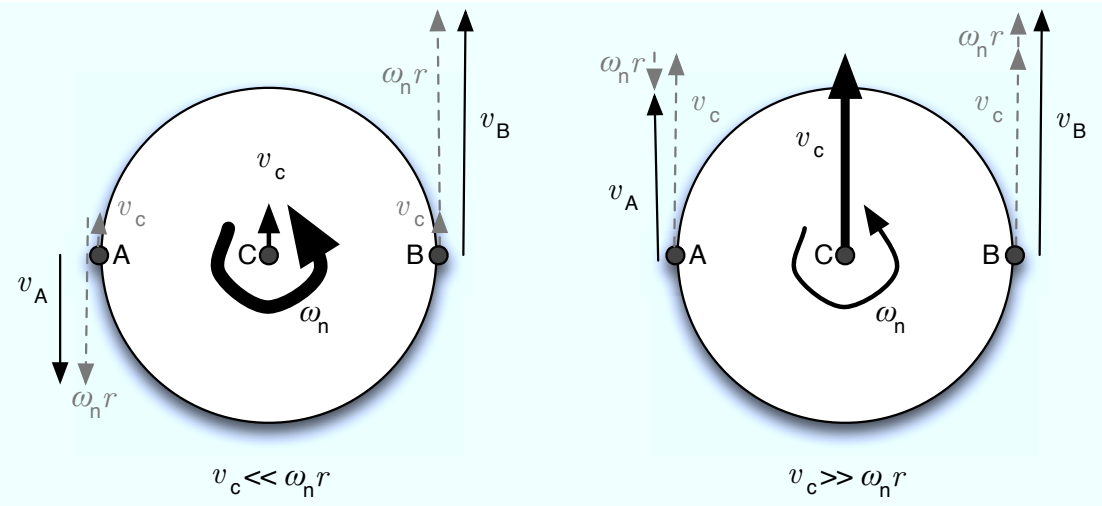

Figure 4.1: The Contensou effect.

Conversely, on the right side of Figure 4.1, it is evident that when v_c is much greater than $\omega_n r$, the tangential motion has the dominant effect on the trajectories of the outer points. Thus, most spinning friction torque will be 'cancelled out.'

Gonthier includes this effect in the volumetric model by introducing a set of dimensionless factors to model the effect of combined translation and rotation [2]. The first Contensou

factor, C_v, is defined as the ratio of tangential speed to average surface velocity:

$$C_v = \frac{|\mathbf{v}_{sct}|}{v_{avg}} \tag{4.31}$$

This factor is used to affect the magnitude of the tangential friction force, so that Equation (4.3) becomes

$$\mathbf{f}_t = -\mu f_n \frac{\mathbf{v}_{sct}}{|\mathbf{v}_{sct}|} C_v \tag{4.32}$$

Thus, if $|\mathbf{v}_{sct}| \gg r_{gyr}|\boldsymbol{\omega}_n|$, full tangential friction is experienced, but if $|\mathbf{v}_{sct}| \ll r_{gyr}|\boldsymbol{\omega}_n|$, tangential friction goes to zero.

The second factor, C_ω is used to affect the magnitude of the spinning friction torque and is given by

$$C_\omega = \frac{r_{gyr}|\boldsymbol{\omega}_n|}{v_{avg}} \tag{4.33}$$

Including this factor in Equation (4.7) gives

$$\boldsymbol{\tau}_s = -\mu r_{gyr}^2 f_n \frac{\boldsymbol{\omega}_n}{|\boldsymbol{\omega}_n|} C_\omega \tag{4.34}$$

Thus, if $|\mathbf{v}_{sct}| \ll r_{gyr}|\boldsymbol{\omega}_n|$, full spinning friction torque is experienced, but if $|\mathbf{v}_{sct}| \gg r_{gyr}|\boldsymbol{\omega}_n|$, friction torque goes to zero.

These factors are applied when the bodies are slipping, but it does not make sense to apply the factors when the bodies are sticking. Thus, Gonthier introduces new terms, $C_{v,s}$ and $C_{\omega,s}$ [1], which are defined as follows:

$$C_{v,s} = s + (1-s)C_v \tag{4.35}$$

$$C_{\omega,s} = s + (1-s)C_\omega \tag{4.36}$$

Equation (4.20) is revised to include $C_{v,s}$

$$\mathbf{f}_f = -f_n \left[\text{sat}\left(\sigma_0 \mathbf{z}_{sc} + \sigma_1 \dot{\mathbf{z}}_{sc}, \mu_{max} C_{v,s}\right) + \sigma_2 \mathbf{v}_{sct}\right] \tag{4.37}$$

Likewise, $C_{\omega,s}$ is included in Equation (4.28) to give

$$\boldsymbol{\tau}_s = -r_{gyr}^2 f_n \left[\text{sat}\left(\sigma_0 \theta_n + \sigma_1 \dot{\theta}_n, \frac{\mu_{max} C_{\omega,s}}{r_{gyr}}\right) + \sigma_2 \omega_n\right] \mathbf{n} \tag{4.38}$$

The bristle dynamics functions, Equation (4.15) and Equation (4.26) must also be updated:

$$\dot{\mathbf{z}}_{sc} = s\mathbf{v}_{sct} + (1-s)\left(\frac{\mu_d}{\sigma_1}\text{dir}(\mathbf{v}_{sct})C_{v,s} - \frac{\sigma_0}{\sigma_1}\mathbf{z}_{sc}\right) \tag{4.39}$$

$$\dot{\theta}_n = s\omega_n + (1-s)\left(\frac{\mu_d C_{\omega,s}}{\sigma_1 r_{gyr}}\text{sgn}(\omega_n) - \frac{\sigma_0}{\sigma_1}\theta_n\right) \tag{4.40}$$

along with their corresponding saturations, Equation (4.21) and Equation (4.27):

$$\dot{\mathbf{z}}_{sc} = \frac{1}{\sigma_1}\text{sat}(\sigma_0\mathbf{z}_{sc} + \sigma_1\dot{\mathbf{z}}_{sc}, \mu_{max}C_{v,s}) - \frac{\sigma_0}{\sigma_1}\mathbf{z}_{sc} \tag{4.41}$$

$$\dot{\theta_n} = \frac{1}{\sigma_1}\text{sat}\left(\sigma_0\theta_n + \sigma_1\dot{\theta}_n, \frac{\mu_{max}C_{\omega,s}}{r_{gyr}}\right) - \frac{\sigma_0}{\sigma_1}\theta_n \tag{4.42}$$

The complete volumetric friction model developed by Gonthier [1] has now been presented.

4.6 Friction Model Parameters

The seven parameters of the volumetric friction model proposed by Gonthier et al. are listed in Table 4.1. State values that are not directly measurable are listed in Table 4.2

Parameter	Description	Units
μ_s	Coefficient of static friction	
μ_d	Coefficient of kinetic friction	
σ_0	Bristle stiffness	m^{-1}
σ_1	Bristle damping	s/m
σ_2	Viscous damping	s/m
τ_{dw}	Dwell-time dependent time constant	s
v_s	Stribeck velocity	m/s

Table 4.1: Volumetric friction model parameters.

Table 4.3 lists model values in addition to those from the normal contact model (Table 2.2) that must be computed from geometries and measured forces and displacements.

State	Description	Units
$\mathbf{z}_{sc}$	Bristle state vector	m
θ_n	Angular bristle state	rad
s_{dw}	Dwell-time dependent stick-slip state	

Table 4.2: Volumetric friction model states.

Value	Description	Units
f_n	Normal force	N
$\mathbf{v}_{sct}$	Contact surface velocity tangent to $\mathbf{n}$	m/s
$\boldsymbol{\omega}_n$	Angular velocity about the normal $\mathbf{n}$	rad/s
v_{avg}	Average surface velocity	m/s
r_{gyr}	Radius of gyration	m

Table 4.3: Volumetric friction model measured quantities.

Chapter 5

Friction Experiments

5.1 Experiments

From the contact model described in the previous chapter, there are three primary modes of motion under friction: pure translational, pure rotational, and combined translation and rotation. In order to simplify the experiments and allow for parameter identification, the experiments have been planned so as to conduct independent translation and rotation first, before observing the Contensou effect under combined translation and rotation.

5.1.1 Pure translational motion

The purpose of using pure translational motion is to determine the seven bristle friction model parameters and to validate that model for the surfaces in contact.

To find the coefficient of static friction, μ_s, the applied force can be increased until the specimen begins to move. The coefficient of static friction is the peak friction force measured at the instant before movement divided by the contact normal force. This should be performed at several different applied normal loads for a more reliable estimate [1].

Gonthier also provides a means of estimating the bristle stiffness parameter [1]. During the initial sticking phase in the model,

$$f_t = -f_n(\sigma_0 z + \sigma_1 \dot{z} + \sigma_2 v_t) \tag{5.1}$$

If speeds are very low,

$$f_t \approx -f_n(\sigma_0 z) \tag{5.2}$$

Thus, if a specimen is slowly accelerated from rest, the bristle stiffness can be estimated as

$$\sigma_0 \approx \frac{\mu_s}{dz} \tag{5.3}$$

where dz is the displacement at the point of peak friction force.

Figure 5.1 shows the ratio of friction force versus normal load for a simulation of the friction model under constant gradual acceleration. Parameters used for the simulation are listed in Table 5.1. It is shown that the peak force ratio comes close to the value used for the static coefficient of friction in the model.

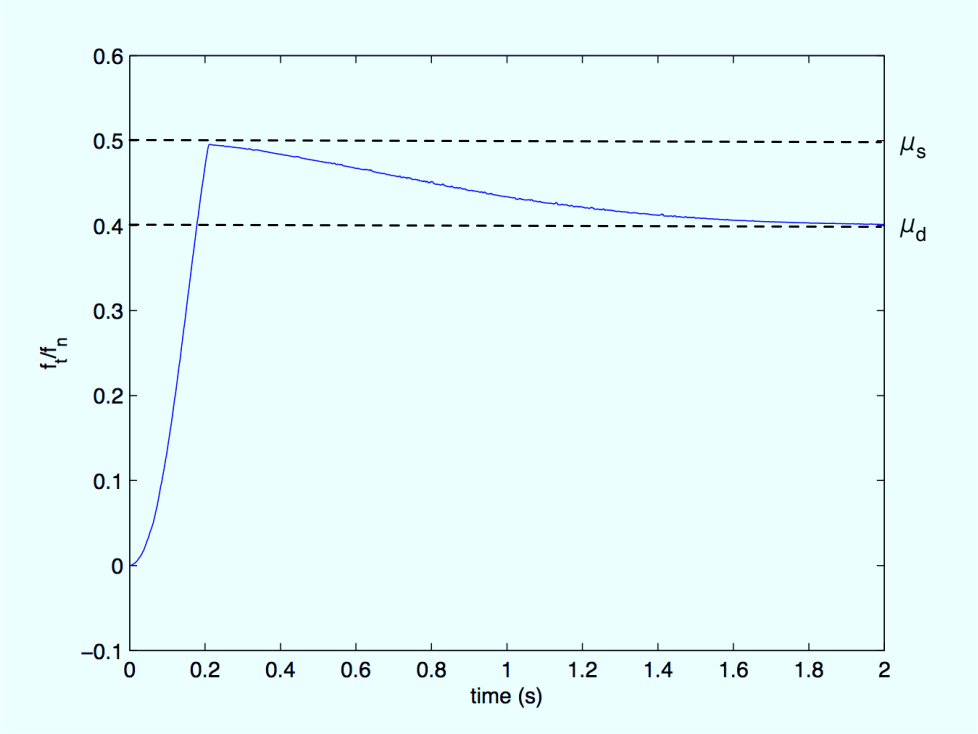

Figure 5.1: Ratio of friction force to normal load for simulation of constant acceleration.

The kinetic Coulomb friction coefficient μ_d and viscous damping coefficient σ_2 can be determined through experiments where the specimen is driven at various different constant velocities [1]. A linear regression of friction force versus applied speeds can be used to

μ_s	μ_d	v_s	σ_0	σ_1	σ_2
0.5	0.4	$10^{-4}\ m/s$	$10^4\ 1/m$	$\sqrt{10^5}\ s/m$	$0\ s/m$

Table 5.1: Simulation parameters.

estimate the coefficients, where the slope of the line yields σ_2, and the y-intercept can be used to find μ_d.

To determine the dwell-time dependency of the materials in contact, the specimen can be driven with sinusoidal velocity profiles of various frequencies, emulating the behaviour of the experiment depicted in Figure 1.3. Peak friction forces will be measured in order to estimate the dwell-time dynamics time constant, τ_{dw}.

Gonthier [1] provides suggestions as to how to find the bristle stiffness and damping parameters, which may be difficult. These values, along with the Stribeck velocity will likely need to be determined through parameter tuning from experiments where the specimen is forced to enter into slipping from rest.

5.1.2 Pure rotational motion

The spinning friction torque model uses the same parameters as those determined by the translational experiments. The main purpose of the rotational experiments is to validate this torque model. Thus, similar experiments can be applied where the specimen is rotated instead of translated to determine if the model fits the data.

5.1.3 Translation and rotation

The purpose of this experiment is to validate the model's description of the Contensou effect. This is achieved by slowly increasing rotational speed while holding the tangential speed constant and measuring the resulting friction forces and torques. The model Contensou factors can then be compared with the measured ones.

5.2 Apparatus

The friction experiments require an apparatus that controls both tangential motion and normal rotation, in addition to applying a contact normal force. The apparatus depicted in Figures 5.2 and 5.3 has been designed to accommodate this. A linear actuator (consisting of a DC brushless motor connected to a ball screw) drives the translational motion, while a small brushless DC motor drives rotation. The specimen is mounted to the shaft of the small motor, the frame of which is mounted through a vertical linear guide to the carriage of the linear actuator to permit free motion in the normal direction.

The specimen was originally intended to be mounted to the motor via a flexible servo coupling of known stiffness which would ensure level contact with the surface. However, it was discovered early on in the experiments that the coupling did not operate as intended. The specimen would lose its vertical orientation as its edge would catch and slip on the surface during translational experiments. The flexible coupling was replaced with a solid aluminum coupling.

As the system is under gravity, the normal force on the specimen is determined from the masses of the motor and specimen. The properties of the volume of interference between the specimen and the contact surface are estimated using the stiffness of the materials and the normal contact model. Since the rotational motor is connected to control and feedback cables, the weight applied to the specimen may shift slightly when the rotational motor is moved by the linear motor, so the applied load must be continuously measured throughout the experiment.

Two 3-DOF (x,y,z) force sensors beneath the contact plate connect it to the ground. These are aligned so that the sensors are centred in the plane of motion of the specimen. The normal force can be measured through the sum of the z-forces, the tangential friction force through the sum of the y-forces, and the spinning friction torque through the difference of the x-forces multiplied by the distance between them.

Alternative designs were considered. A four-axis CNC would enable the desired motion; however, concerns over control and real-time position measurement made such a choice unfeasible. In addition, many CNC designs would require the contact plate to be moved to enable relative motion with respect to the specimen, the accelerations of which would register on the force sensors. Parallel manipulators were also considered, but were considered

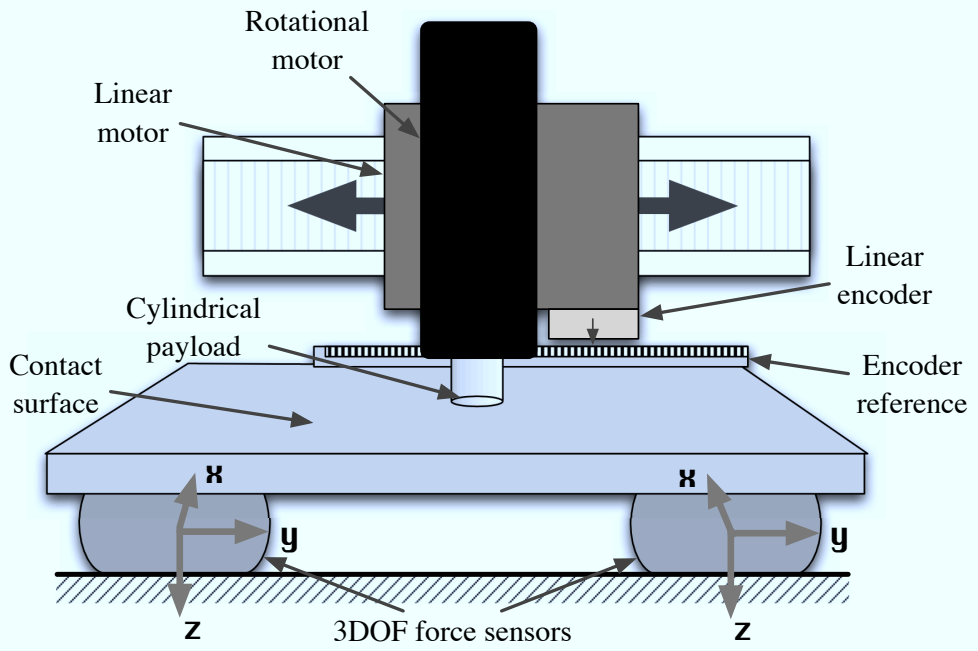

Figure 5.2: Diagram of apparatus for friction experiments.

to be limited in their range of motion and might require more effort to ensure independent translational and rotational experiments.

5.3 Results and Discussion

5.3.1 Translational motion

Static friction experiment

As described in 5.1.1, determining the static parameters of the model requires taking measurements while driving a 10 mm diameter titanium specimen from rest. For this experiment, the linear motor was commanded to give a constant acceleration of 0.1 mm/s^2, while the smaller motor did not rotate.

For the purposes of analysis, the ratio of friction force to normal force magnitudes, given by

$$\mu = \frac{f_t}{f_n} \tag{5.4}$$

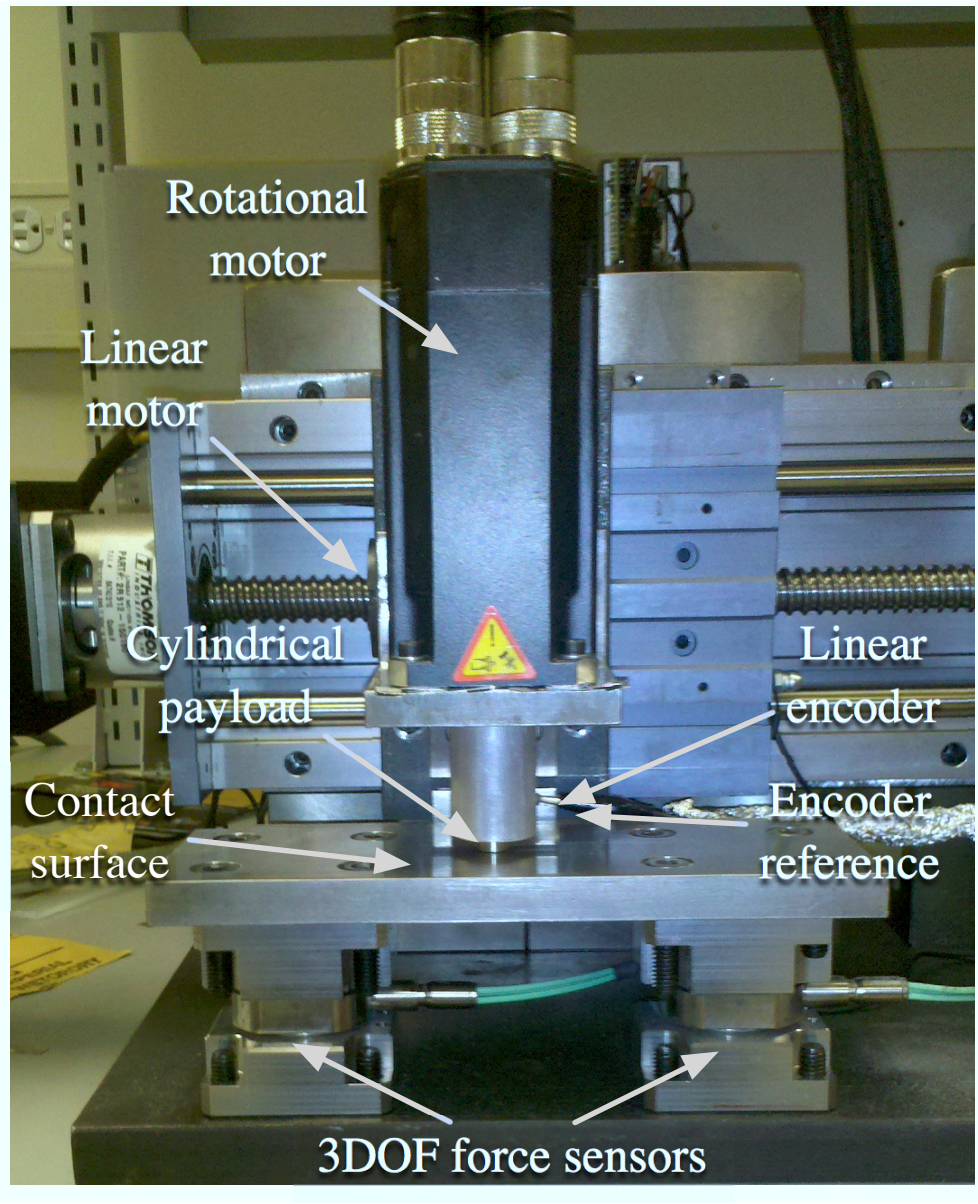

Figure 5.3: Apparatus for friction experiments.

will be referred to as the *instantaneous* coefficient of friction. The instantaneous coefficient of friction over 0.5 mm of motion is presented in Figure 5.4.

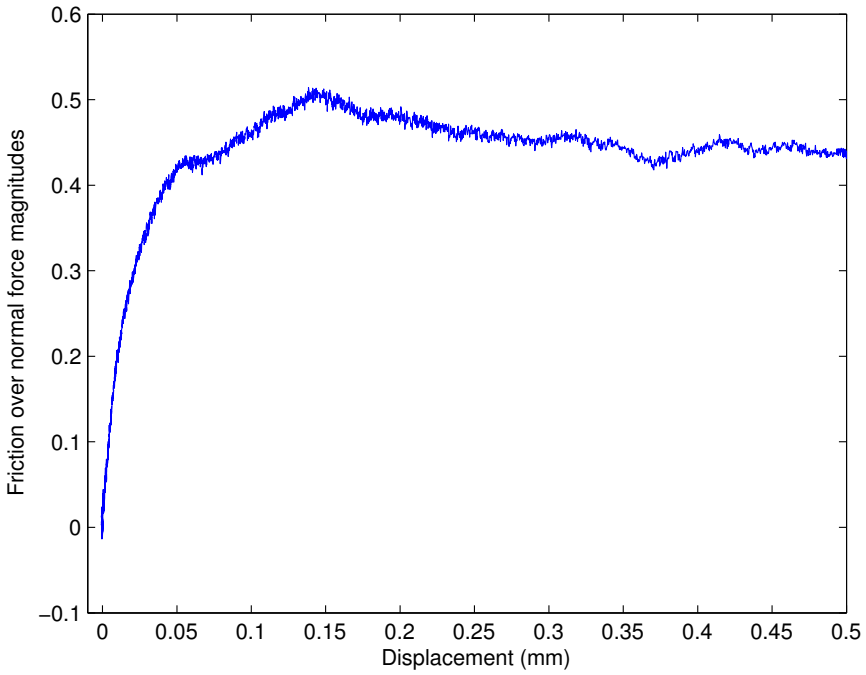

Figure 5.4: Instantaneous coefficient of friction versus displacement for 0.1 mm/s^2 acceleration of 10 mm titanium specimen from rest.

Peak friction occurs at 144 μm of displacement with an instantaneous coefficient of 0.51. Following Equation (5.3), which assumes a linear fit, the bristle stiffness σ_0 is estimated to be 3.5×10^3 $1/m$. The slope of the curve in Figure 5.4 decreases significantly around 50 μm.

From Equation (5.2), it is expected that the relationship between displacement and instantaneous coefficient be close to linear prior to peaking. This expectation is not met by the experimental results. If bristle stiffness were measured from an earlier point before the peak, the estimate would be an order of magnitude higher.

Moving the specimen over the contact surface resulted in scratches to both surfaces, shown in Figure 5.5. Small pits and markings appeared along the wear lines, indicating that the surface was not consistent along the line of motion. Figure 5.6 shows the instantaneous

coefficient of friction over 8 mm of travel at a constant velocity of 1 mm/s from one experiment. The amount of friction is not constant but fluctuates as the specimen 'catches' on the pits and scratches. Thus, some of the measured friction forces are not the result of the interaction between microscopic 'bristles', but of larger and more visible imperfections in the surfaces.

Figure 5.5: Wear to the titanium flat surface left by the 10 mm titanium specimen.

Additionally, as new scratches are formed with each motion, the interactions between the surfaces are not entirely elastic, but partially plastic. This may explain the reduction of slope in the friction coefficient curve in Figure 5.4, as the contact surfaces strain plastically.

To reduce the likelihood of plastic deformation, it was necessary to reduce the force concentration on the contact surface. Little could be done to reduce the normal load on the specimen, since most of the weight was in the rotational motor to which it was mounted. Increasing the diameter of the specimen from 10 mm to 25.4 mm would increase the contact surface area by over a factor of six and reduce pressure by the same factor. A 25.4 mm diameter specimen was made from aluminium. Aluminium was selected because it was more compliant than the titanium testbed so that if plastic deformation did take place, it would occur in the specimen, which was easier to replace.

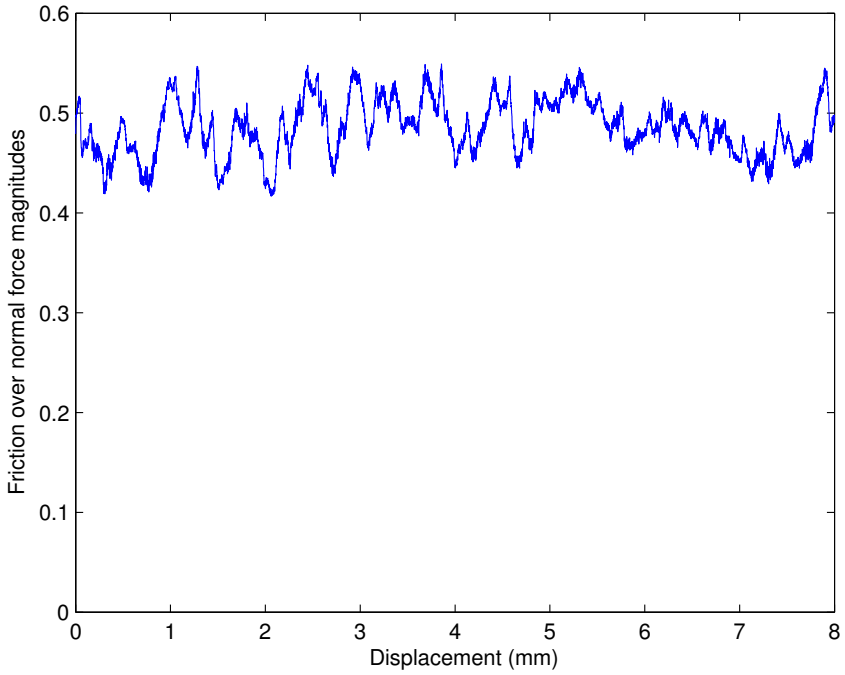

Figure 5.6: Instantaneous coefficient of friction versus displacement for constant velocity of 1 mm/s for 10 mm titanium specimen.

Using the same acceleration of 0.1 mm/s^2, the experiment was repeated with the aluminum specimen. Results are shown as a solid line in Figure 5.7. It is first observed that there is substantially less friction for this larger aluminum specimen than with the smaller titanium one. Aluminum is more compliant than titanium, so it is not surprising that the 'bristles' in the aluminum surface give less resistance. Additionally, the wear that resulted in the experiments with the smaller specimen suggests that visible imperfections, in addition to microscopic bristles were having to deform so that the titanium specimen could move.

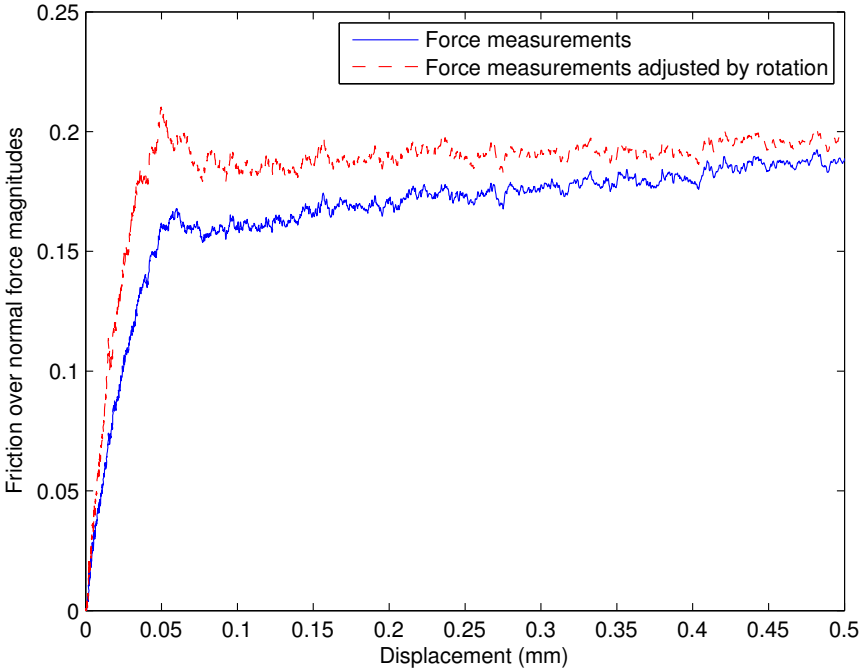

Figure 5.7: Instantaneous coefficient of friction versus displacement for 0.1 mm/s^2 acceleration of a 25.4 mm aluminum specimen from rest.

It is noted that the 'peak' also occurs 0.5 mm from rest. However, after the friction peaks and declines slightly, the friction forces rise gradually as the specimen continues to accelerate. This trend in Figure 5.7 is distinct from the trend with the smaller specimen in Figure 5.4, as friction increases linearly with displacement during the stick-slip transition and there is an observable decline following the peak.

Encoder measurements from the rotational motor were also taken. These measurements indicated the specimen would rotate up to 2 degrees during stick-slip transition. (The motor could not be locked, but was commanded to maintain a 'zero' position. If a disturbance was introduced, following error could occur.) Angular positions from the above experimental run are shown in Figure 5.8. Since there is rotation taking place during the transition, one might expect the Contensou effect to reduce the amount of friction experienced.

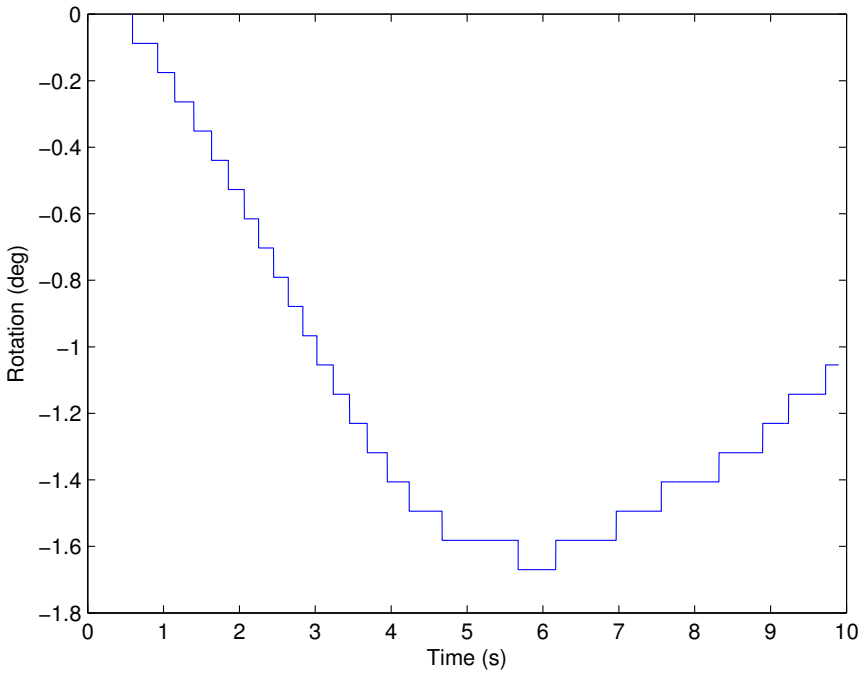

Figure 5.8: Rotary encoder measurements from translational static friction experiment.

The dimensionless Contensou factor C_v can be applied, where

$$f_t = \mu f_n C_v \tag{5.5}$$

to give a new expression for μ:

$$\mu = \frac{f_t}{f_n C_v} \tag{5.6}$$

The adjusted coefficient of friction calculated with (5.6) is presented as a dashed line in Figure 5.7. Compared with the 'raw' coefficient of friction, there is a clearer peak

followed by tapering and leveling off as static friction is overcome and slip begins. For this experiment, the volumetric contact model's Contensou factor provides a good description of friction behaviour when slight rotation occurs during translation.

Experimental plans called for testing with different normal force loads. However, the setup only allowed for increasing the load, and it was thought that further increasing the normal force pressure would lead to greater wear of the contact surface. Instead, different accelerations were tested.

Experiments were repeated for accelerations ranging from 0.1 to 0.5 mm/s^2. Each experiment yielded similar coefficient of friction profiles to that of Figure 5.7. The peak coefficients were recorded and are shown in Figure 5.9. The mean coefficient of static friction was 0.204.

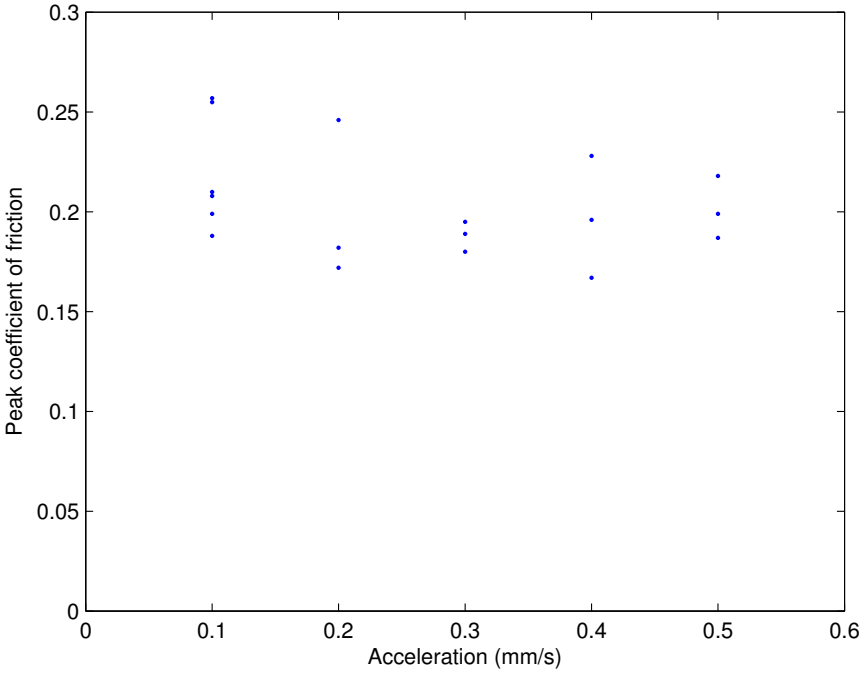

Figure 5.9: Peak coefficients of friction for various linear accelerations.

There is a significant amount of variability in measuring the static coefficient of friction. As the experiments progressed, the testbed surface appeared increasingly scratched, though not as deeply as with the smaller specimen. The extent of the wear is shown in Figure 5.10.

Thus, the contact surfaces changed with each experiment due to permanent deformations that were taking place. Further experiments are therefore required, with lowered contact pressure so that visible surface changes do not occur.

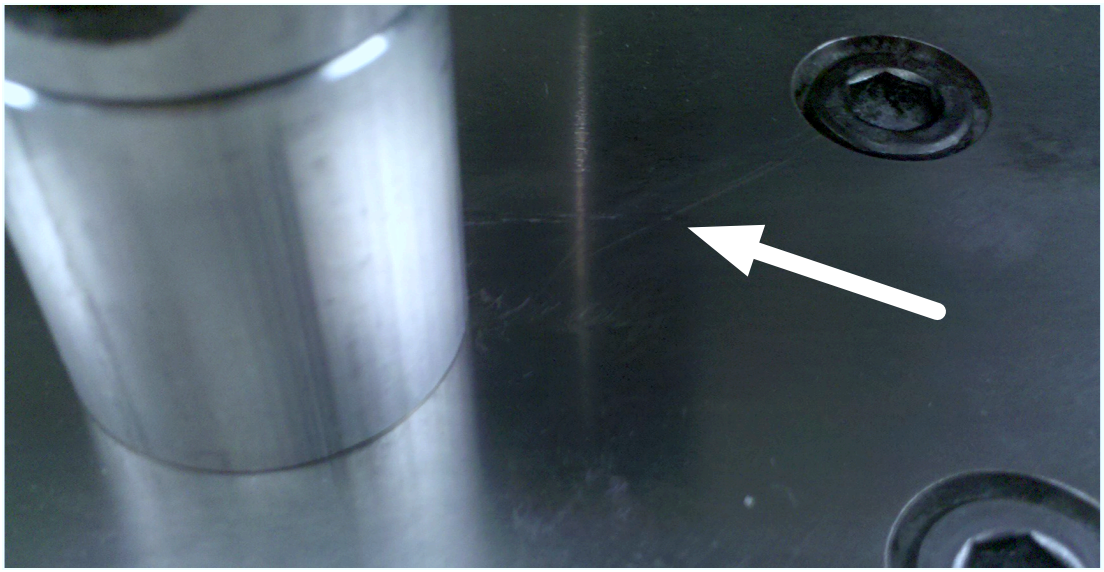

Figure 5.10: Wear to the titanium surface from the 25.4 mm aluminum specimen.

Using Equation (5.3), the bristle stiffness σ_0 could be estimated for each of the experiments. The average distance travelled before peak force was achieved was 46 μm, and the average bristle stiffness was 4500 m^{-1}.

With an estimate for σ_0, the bristle damping parameter σ_1 could be estimated. During the sticking phase, the bristle state $\mathbf{z}_{sc}$ and speed $\dot{\mathbf{z}}_{sc}$ are approximately equivalent to the total displacement and speed of the specimen, respectively. Thus, we can write the model friction coefficient during this phase as

$$\mu \approx \sigma_0 d_t + \sigma_1 v_t \tag{5.7}$$

where d_t is the tangential displacement of the specimen from the rest position. A bristle damping coefficient σ_1 was estimated using measurements prior to friction peaking for each experiment. Figure 5.11 shows the measured friction alongside model values with and without damping for an acceleration of 0.1 mm/s^2. There is good agreement between the model and results when bristle damping is introduced. The average bristle damping σ_1 was 300 s/m.

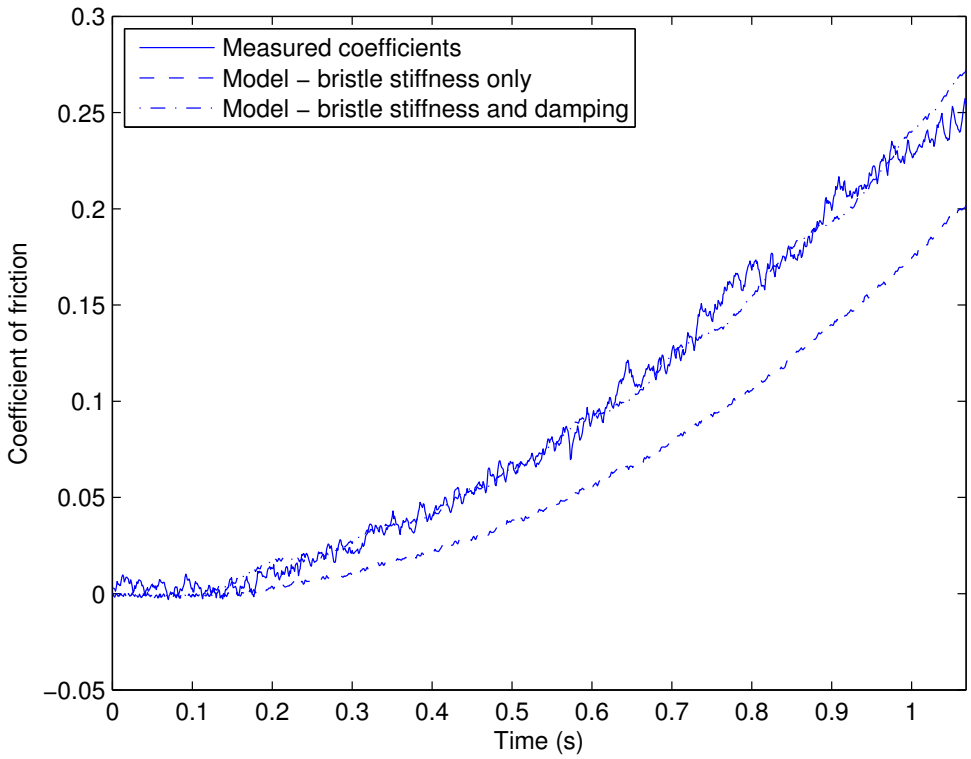

Figure 5.11: Estimate of bristle stiffness and damping parameters (σ_0 and σ_1).

Since increasing the weight on the specimen would only lead to further damage to the contact surface, experiments with different applied normal forces were not performed. The stainless steel spherical specimen was also not used, as it was assumed that the small contact patch and resulting concentrated high pressures would lead to even deeper scratches to the surface.

Dynamic friction experiments

The larger aluminum specimen was driven at different constant velocities, ranging from 0.5 mm/s to 2.5 mm/s to estimate coefficients of kinetic friction, μ_d, and viscous friction, σ_2. For the slipping case,

$$f_t = f_n(\mu_d + \sigma_2 v_t) \tag{5.8}$$

Combining Equation (5.4) with Equation (5.8) gives a linear relation between μ and v_t:

$$\mu = \mu_d + \sigma_2 v_t \tag{5.9}$$

This allows the slipping friction parameters to be estimated through linear regression of measured coefficients of friction and velocity.

As with the static friction experiments, wear to the contact surface with the larger specimen was still observed. In addition, great variability in the measured coefficient of friction was observed, as shown in Figure 5.12. The peaks in friction coefficients were assumed to represent points where the visible scratches in the two contact surfaces would catch on each other, while the declines that follow represent when the scratches break free of each other.

Averages of measured coefficients are plotted by speed in Figure 5.13. A linear regression is shown as a solid line. The y-intercept and slope, which are our estimates for μ_d and σ_2, are 0.187 and 10.4 s/m, respectively. However, the quality of the regression is poor, as the coefficient of determination, R^2, is only 0.085. Thus, it is difficult to give a certain value for the kinetic coefficient between the aluminum and titanium that is more precise than 0.2, or to say definitively that viscous friction is taking place.

The variability in the measurements of the coefficient of friction likely stem from the plastic deformations to the metallic surfaces over the course of the experiments. Thus, the surfaces did not remain the same between experiments. These changes in surface roughness

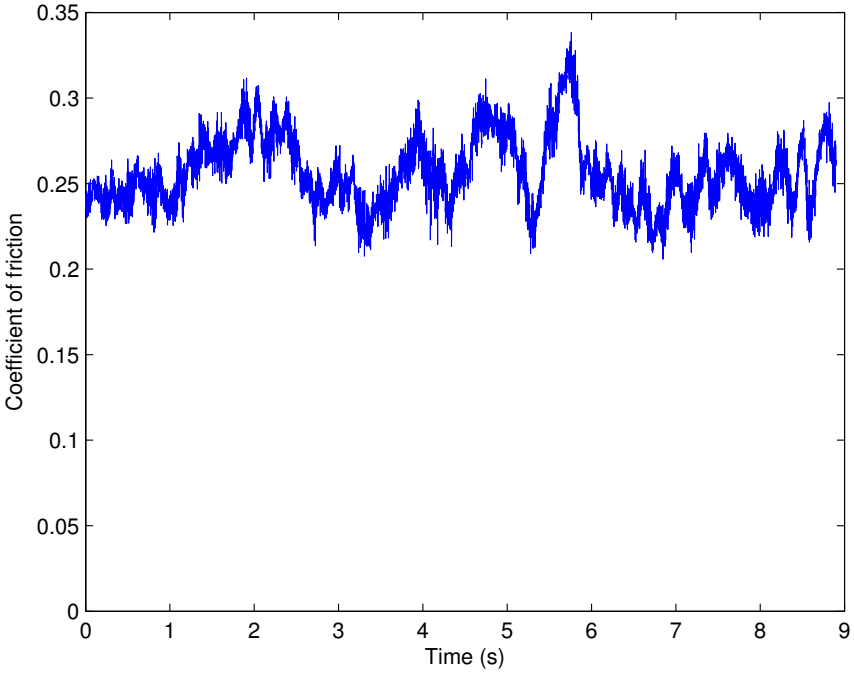

Figure 5.12: Coefficients of friction over time for motion at a constant speed of 1.8 mm/s.

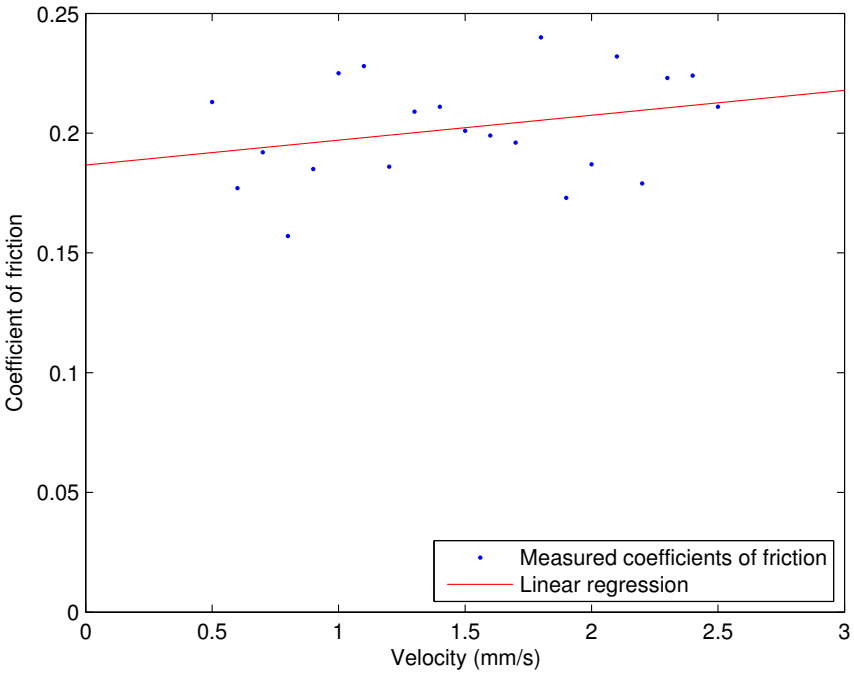

Figure 5.13: Mean coefficients of friction versus constant velocity travelled.

led to changes in observed coefficients of restitution. In this case where wear takes place, the static and kinetic coefficients of friction are difficult to measure as distinct parameters. This makes any attempt to determine the Stribeck velocity v_s difficult, as there is no clear distinction between slipping and sticking.

Dwell-time dependency experiments

As both static and dynamic experiments yielded similar estimates for static and kinetic coefficients of friction for the aluminum specimen on the titanium surface, and measured values yielded a high degree of variability, it was not anticipated that dwell-time dependency for these materials could be observed or measured. However, the proposed dwell-time experiments were still conducted.

The experiment involved applying a sinusoidal motion pattern to the specimen at various frequencies. Figure 5.14 shows the sticking state function s and dwell-dependent state s_{dw} in simulation, with an arbitrary dwell-time constant τ_{dw} of 0.3. From Equation (4.30), if s_{dw} is close to 1, (i.e. sticking), the effective coefficient of friction will be closer to the higher value of μ_s, while if it is close to 0, (i.e. slipping), the coefficient will be closer to μ_d.

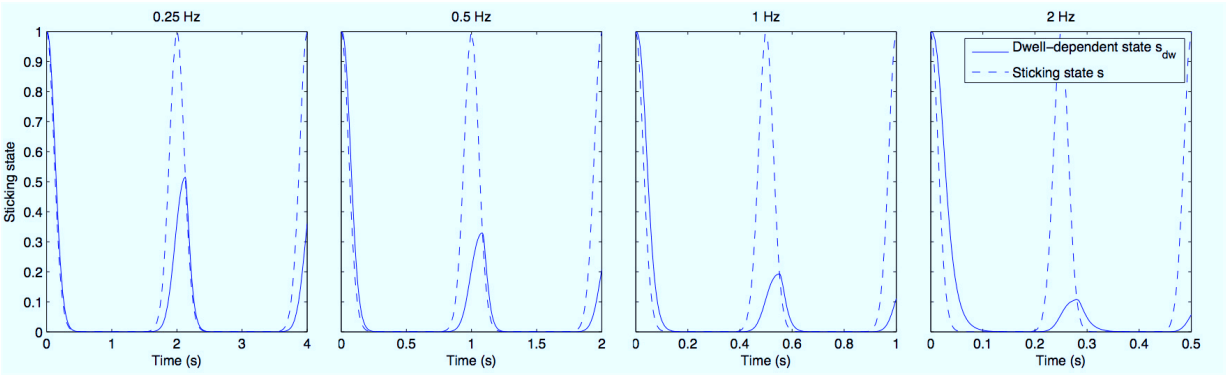

Figure 5.14: Simulated sticking state for oscillating motion starting from rest.

From these simulated results, it is apparent that for a lower frequency like 0.25 Hz, the peak friction forces with each oscillation will be roughly halfway between the maximum static friction $\mu_s f_n$ and kinetic friction $\mu_d f_n$. For higher frequencies such as 2 Hz, there is insufficient time when the specimen comes to rest for it to begin sticking again, so peak friction forces will barely exceed kinetic friction levels. Thus, higher frequencies should

yield lower peak friction values, while lower frequencies should lead to greater amounts of friction.

The linear motor was directed to follow a sinusoidal motion at frequencies of 0.25, 0.5, 1, and 2 Hz, achieving a maximum speed of 2 mm/s. Since the specimen was moving back and forth, each subsequent cycle would be along the 'same' surface (though it is understood from the previously observed wear that the surface does in fact change).

Actual measurements reveal that the amount of friction experienced by the specimen actually increases above the initial peak, instead of decreasing, as might be expected from the dwell-time dependent model. Figure 5.15 shows the measured coefficients of friction for 0.25 Hz. Friction in the initial stick-slip transition achieves a peak coefficient of 0.2, but can exceed 0.4 in later oscillations. This effect was also observed at higher frequency oscillations.

Increased forces under oscillation are often attributed to resonance at natural frequencies. However, position measurements closely track the commanded motion, so instability is unlikely. In addition, the oscillating frequencies are very low compared to the natural frequencies of the sensors (3.6 kHz).

Wear to the surface is also considered as a possible cause of the observed increase in friction forces. It was thought that the specimen might be 'digging' grooves into the contact surface, which could lead to greater friction with each pass. However, the initial peak friction always began around 0.2 when experiments were repeated at the same location on the contact surface, so whatever the effect, it is not permanent.

Temperature at the contact site was also considered, though it could not be directly measured. It is likely that the friction was generating some heat, especially as the specimen was moving back and forth over a small area. This added heat could serve to increase the adhesiveness of the surfaces. There was sufficient time to cool between experiments, which would restore the maximum friction coefficient to around 0.2.

It can therefore be hypothesized that friction forces between metals are dependent on the temperature of the surfaces in contact, including the heat generated by the same friction between the bodies.

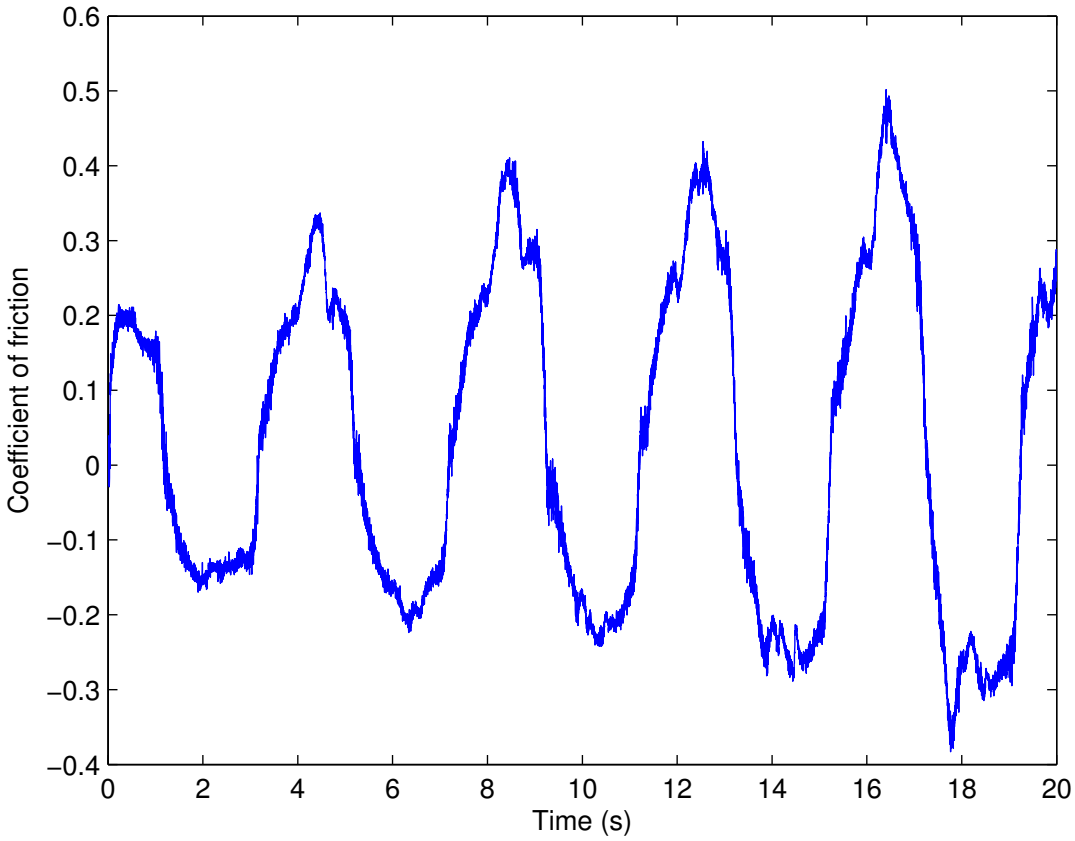

Figure 5.15: Measured coefficient of friction from oscillation of 0.25 Hz.

5.3.2 Rotational motion

As with the translation experiments, the larger aluminum specimen was used for measurements with rotational motion. The larger specimen provided a larger radius of gyration which should serve to increase the magnitude of the friction torque measured, yielding more reliable results.

Friction torque is measured through the reaction forces along the x-direction (Figure 5.2) at the two force transducers rigidly mounted to the contact surface. These sensors are rigidly fixed to the ground, allowing the contact plate to be modelled as a beam fixed at both ends. Reaction forces, which can be measured directly, are shown in Figure 5.16 as F_{x1} and F_{x2}. Moments M_1 and M_2 are reactions required to prevent the contact plate from rotating at the mounting points, which cannot be directly measured through the sensors. Using beam theory, the friction torque can be given by [24]

$$\tau_s = \frac{L^3}{12y(L-y)}\left(F_{x1} - F_{x2}\right) \tag{5.10}$$

where y is the distance from sensor 1 to the centre of rotation for the specimen, as shown in Figure 5.16.

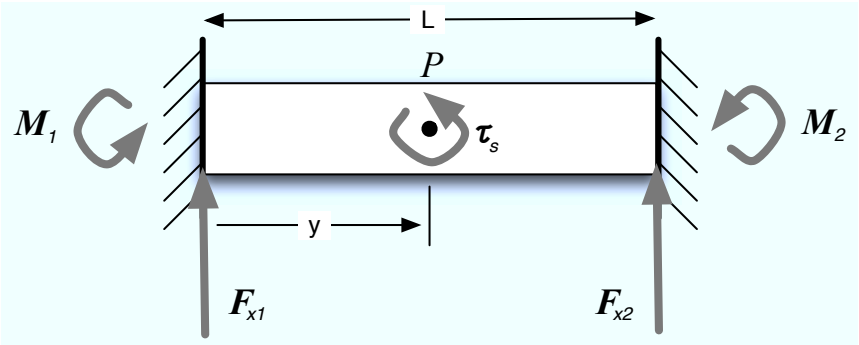

Figure 5.16: Reaction forces to spinning friction torque.

For the case where the specimen is at the midpoint between the sensors,

$$\tau_s = \frac{L}{3}\left(F_{x1} - F_{x2}\right) \tag{5.11}$$

Equation (5.11) will be used for the rotational friction experiments, since the specimen will be situated at the centre of the apparatus and will not be moving laterally. Equation (5.10)

can be used in the following section on Contensou effect experiments, where the specimen is undergoing both rotational and translational motion.

For rotation, Equation (4.28) can be simplified to give the effective coefficient of friction

$$\tau_s = r_{gyr}\mu f_n \tag{5.12}$$

This can be rearranged to give

$$\mu = \frac{\tau_s}{r_{gyr} f_n} \tag{5.13}$$

The encoder from the motor provided very coarse measurements, as was seen in Figure 5.8. Resolution was 0.087° per encoder step. This was unsatisfactory for small rotations, such as in the static friction experiments, so angular measurements were smoothed using a moving average of the nearest 100 samples.

Static friction experiments

The specimen was put through angular accelerations from 0.005 to 0.025 rad/s^2. The measured coefficient of friction was found to peak within the first 1° of rotation. Figure 5.17 shows results from one experiment, with an acceleration of 0.025 rad/s^2.

From the figure, a peak in friction is seen soon after the specimen begins to move. The relationship between rotation and friction does not appear to be linear in the initial sticking phase, though it should be noted that the peak occurs after only about 2 encoder steps of motion. Once slip occurs, the decrease in friction torque appears more significant than that of the translational friction forces in Figure 5.7 of the previous section.

Lateral displacement of the specimen was also measured, but was determined to be too low (i.e. less than 10 $\mu m/s$) to produce any measurable impact on friction torque through the Contensou effect.

Peak friction coefficients μ_s determined from accelerations of 0.005 to 0.025 rad/s^2 are shown in Figure 5.18. As with the translational friction, there is a high amount of variability in the measurements. The mean coefficient of friction was found to be 0.205, which is close to the value of 0.204 found for translational friction.

Due to the coarseness of the angular measurements during the sticking phase, estimates for the parameters σ_0 and σ_1 were not determined. Peak friction appears to occur near 0.01 rad/s in most cases.

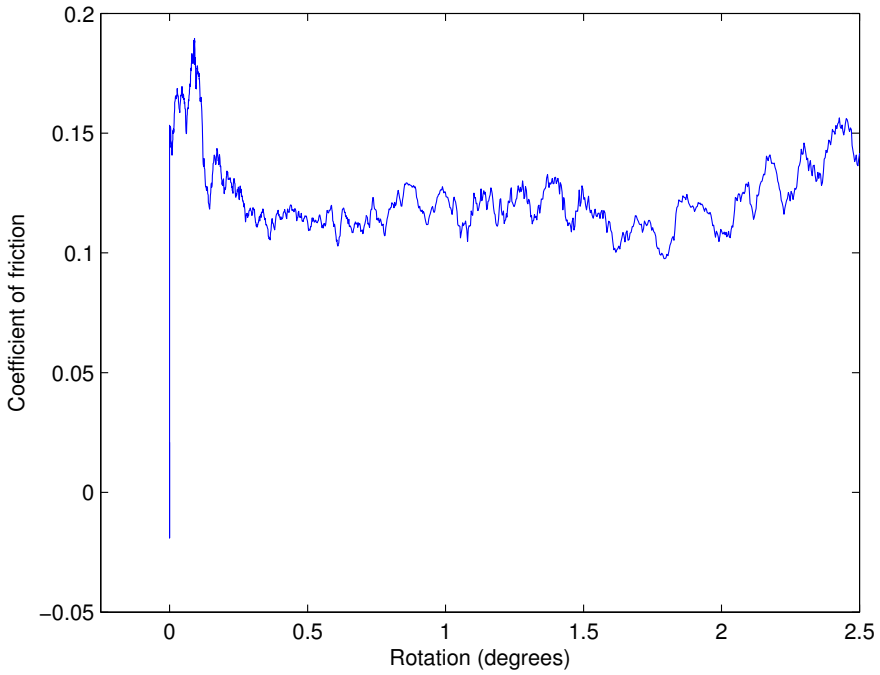

Figure 5.17: Instantaneous coefficient of friction versus angular displacement for 0.025 rad/s^2 angular acceleration of a 25.4 mm aluminum specimen from rest.

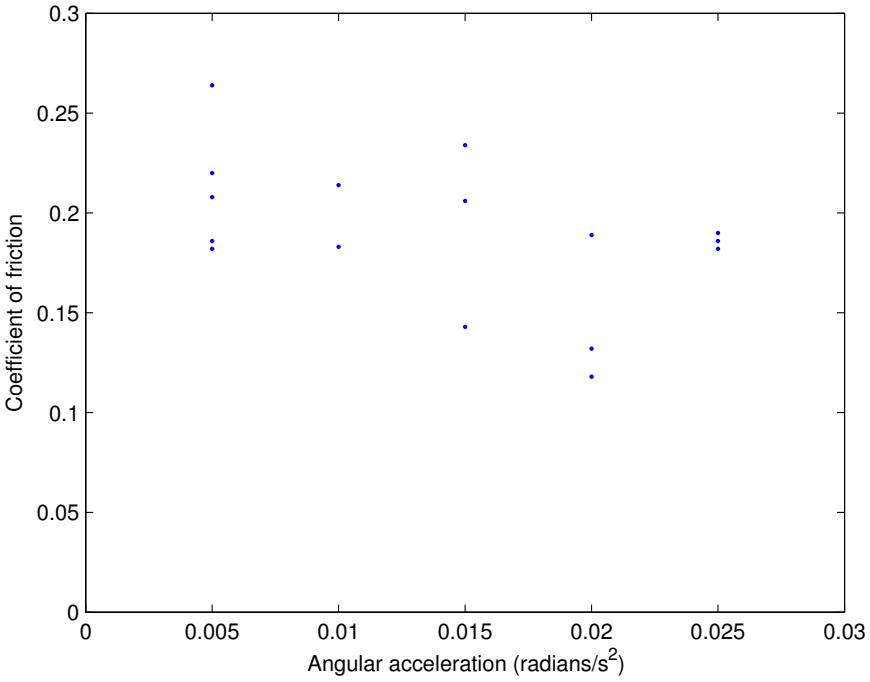

Figure 5.18: Peak coefficients of friction for various angular accelerations.

As with the translational experiments, wear to the contact surfaces took place when the specimen was rotated. Scratch marks can be seen as the larger arcs in Figure 5.19. There is also significant marring to the surface at the end of the lower arc. The surface is still undergoing significant changes between experiments, explaining the variability in results. The deeper scratches may also explain the rapid decline in friction observed in Figure 5.17. As the specimen is forced by the motor to rotate, it breaks free of the grooves in the surface.

Figure 5.19: Large circular scratch pattern left by rotational experiments with aluminum specimen.

Dynamic friction experiments

The larger aluminum specimen was driven at different constant angular velocities, ranging from 0.05 to 0.25 rad/s to estimate coefficients of kinetic friction μ_d and viscous friction σ_2. Considering Equation (4.28) for pure slipping,

$$\tau_s = r_{gyr}^2 f_n \left(\frac{\mu_d}{r_{gyr}} + \sigma_2 \omega_n \right) \tag{5.14}$$

Combining Equation (5.12) and Equation (5.14), we find a linear equation in ω_n, yielding the effective coefficient of restitution,

$$\mu = \mu_d + (r_{gyr}\sigma_2)\omega_n \tag{5.15}$$

As with the previous experiments, scratches to the contact surface with the larger specimen were still observed. In addition, great variability in the measured coefficient of friction was observed, as shown in Figure 5.20. The peaks in friction coefficients were assumed to represent points where the visible scratches in the two contact surfaces would catch on each other, while the declines that follow represent when the scratches break free of each other.

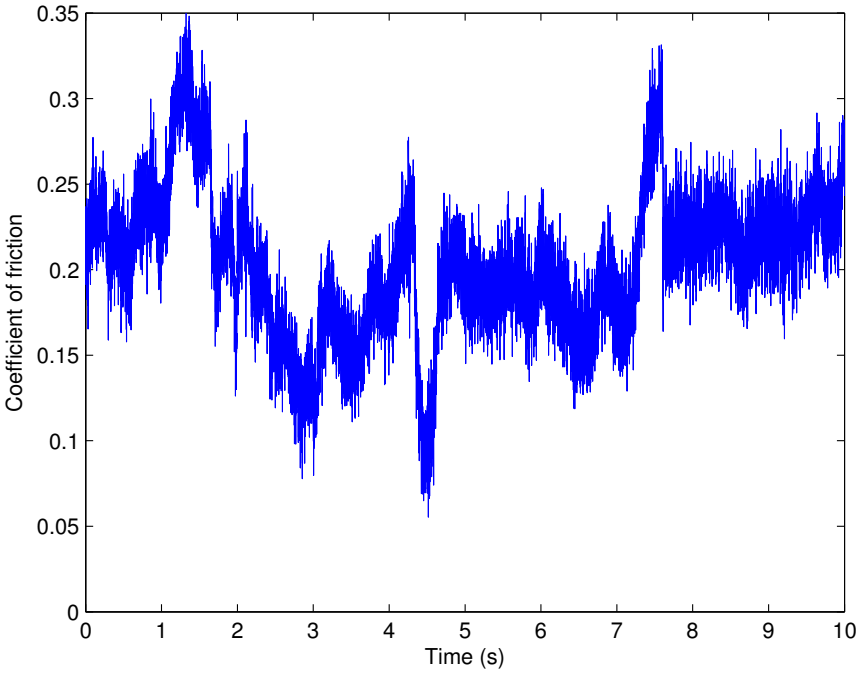

Figure 5.20: Coefficients of friction over time for motion at a constant angular velocity of 0.21 rad/s.

Average measured coefficients are plotted by speed in Figure 5.21. A linear regression is shown as a solid line. The y-intercept and slope, which are our estimates for μ_d and $r_{gyr}\sigma_2$, are 0.177 and 0.154 s, respectively. This gives an estimate for σ_2 of 17.1 s/m, which is of

the same order of magnitude as for the tangential experiments, 10.4 s/m. The estimate for μ_d is also very close to that of the tangential case, 0.187.

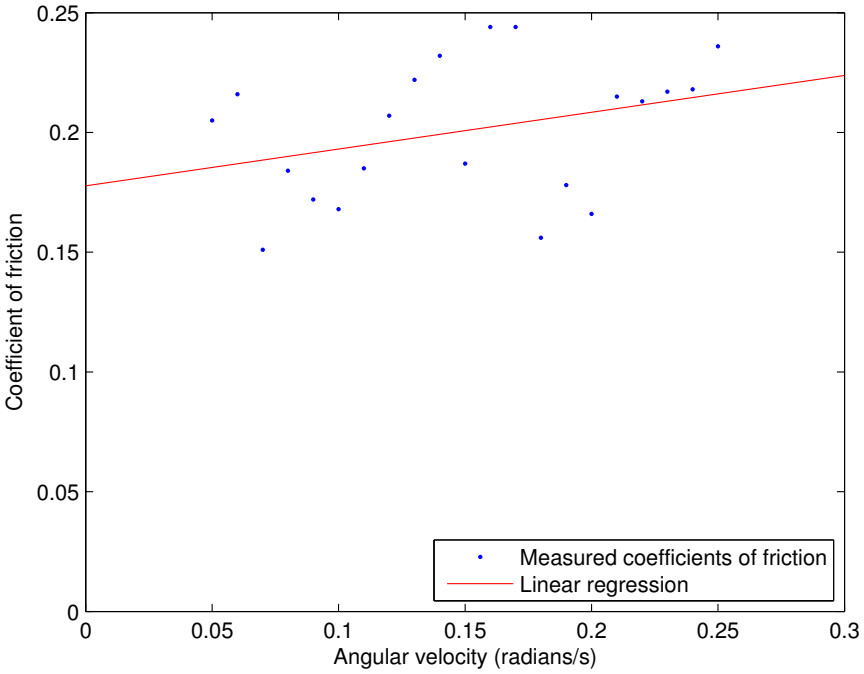

Figure 5.21: Mean coefficients of friction versus constant angular velocity.

However, the quality of the regression is poor, as the coefficient of determination, R^2, is only 0.11. As with tangential friction, it is difficult to give a certain value for the kinetic coefficient between the aluminum and titanium that is more precise than 0.2, or to say definitively that viscous friction is taking place.

5.3.3 Translation and rotation

The Contensou effect was already observed in Section 5.3.1. The following experiment explored this effect further. The aluminum specimen was driven at a constant tangential velocity of 2 mm/s, while undergoing an angular acceleration of 0.1 rad/s^2. Normal and friction forces and spinning friction torques were measured to determine coefficients of friction during the experiment. Tangential and angular speeds were also measured in order

to determine the impact of the Contensou effect.

The observed frictional coefficient in the tangential direction, measured using Equation (5.4), is shown in Figure 5.22. The specimen was undergoing translational motion with a coefficient of about $\mu = 0.4$ when the angular motor began to accelerate. The tangential Contensou factor C_v was determined with the velocity and angular velocity measurements using Equation (4.31). The model value μC_v is shown as a dashed line in the figure. The Contensou factor is shown to provide a very close estimate of the impact of rotation on the tangential friction experienced.

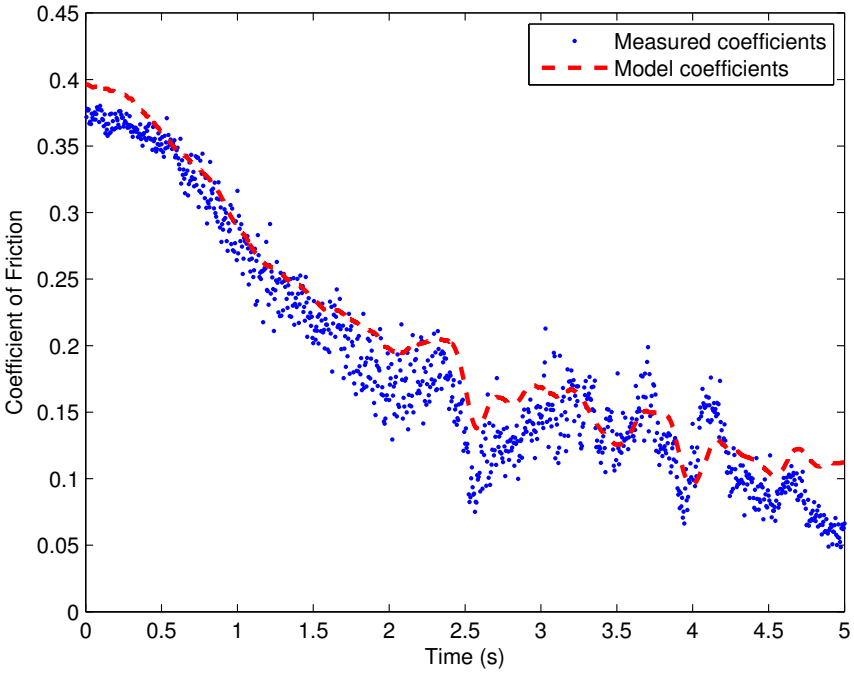

Figure 5.22: Translational friction measurements for constant velocity and accelerating angular velocity.

Coefficients of friction were also measured from the torque measurements, and are shown in Figure 5.23. The angular Contensou factor C_ω was determined using Equation (4.33). The model value μC_ω is shown as a dashed line in the figure. The model provides a reasonable estimate of friction for the first two seconds of angular acceleration. Between 2-5 s, the measured coefficients fluctuate quickly compared with the model. From Figure 5.24,

which shows measured angular velocities for the experiment, it is clear that the angular velocity also fluctuate rapidly during this period of time. These rapid changes in velocity may be affecting friction forces in a manner that the Contensou model does not account for.

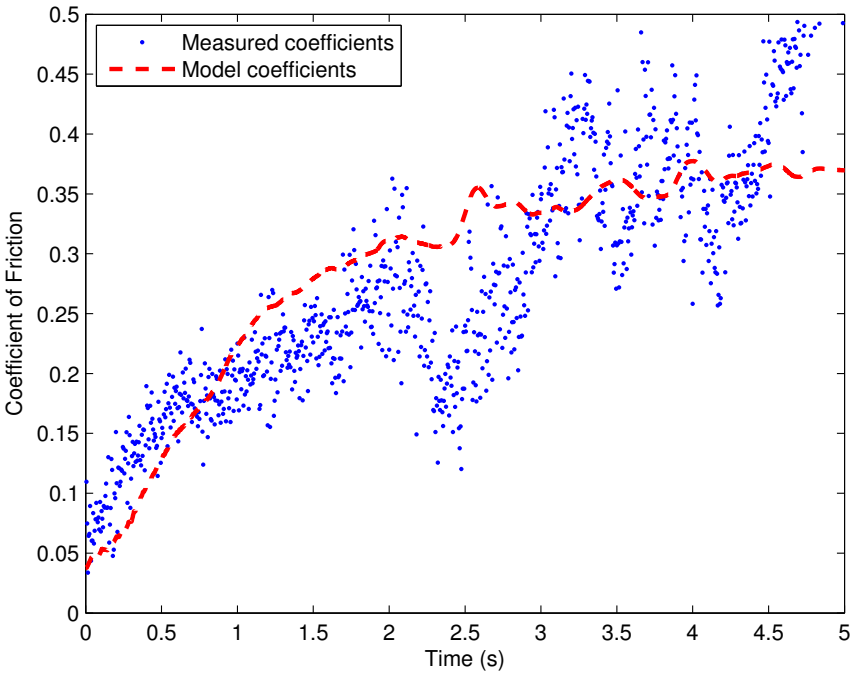

Figure 5.23: Spinning friction measurements for constant velocity and accelerating angular velocity.

The Contensou effect is clearly observed from this experiment. The Contensou factors C_v and C_ω are shown to provide reasonable estimates of the impact of combined rotation and translation on the friction forces experienced.

5.3.4 Limitations of experiments

Plastic deformation of contact surfaces

As noted in Figure 5.5 and Figure 5.19, a significant amount of plastic deformation took place over the course of the experiments in the form of scratches to the contact surfaces.

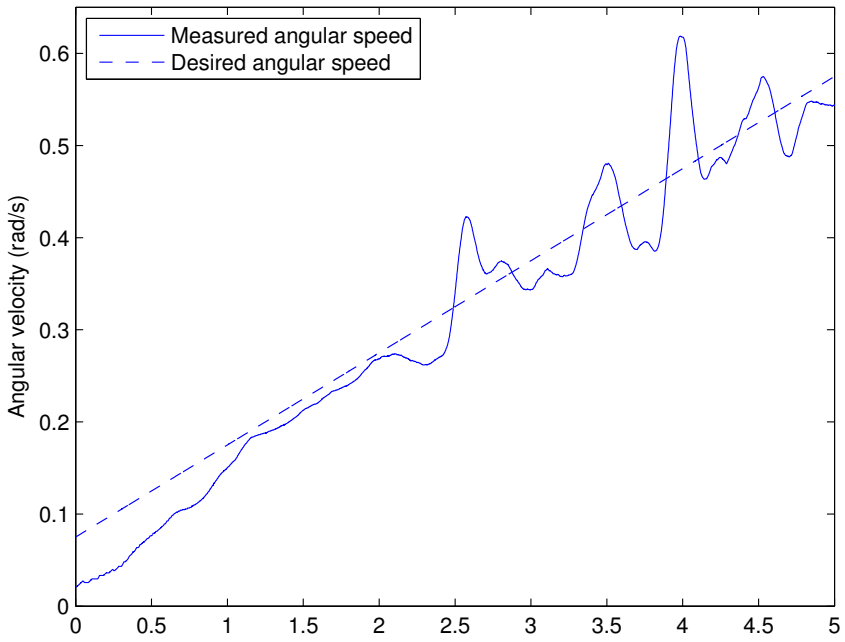

Figure 5.24: Angular velocity of specimen for Contensou experiment.

This meant that the surfaces changed from experiment to experiment. Replacement of the contact surfaces between experiments would have required expensive manufacture of titanium components. Also, as the linear encoder reference was mounted to the lower contact surface, reconfiguration and recalibration with each replacement of contact components would be required.

It was discovered that the wear on the contact surfaces generated a fine metallic dust. This dust was wiped away with a cloth between each experiment.

Alignment

Alignment of the specimen with the contact surface was initially attempted using a flexible coupling. This coupling presented two significant limitations. First, it failed to keep the specimen perfectly flat, instead causing the orientation of the specimen to change as it dragged across the contact surface, so that part of the time it was only catching on one edge. Second, it introduced flexibility between the contact site and the position measurements. This compliance interfered with the measuring of the bristle stiffness and damping.

For the experiments, the flexible coupling was replaced with a solid aluminum coupling. This allowed bristle parameters to be measured more accurately, while maintaining a fixed vertical orientation. The mounting of the rotary motor was manually configured such that the specimen would rest flat on the surface. However, since the wear was not uniform on the contact surface and was more prevalent on the one side, (Figure 5.5), it is apparent that the pressure from the normal force was not uniform across the surface of the specimen.

Compliances

The apparatus was designed such that the displacement measurements would capture primarily the strain within the contacting materials. Thus, the position encoder was placed in proximity to the specimen mounting hardware and the reference was mounted directly behind the contact surface. However, there is the possibility of some compliance within the mounting bracket of the rotary motor and in the motor axis itself. These compliances could serve to decrease the magnitude of the bristle stiffness parameters estimated.

Dynamic response of the force sensor

It was important that the dynamic behaviour of the force transducer not affect the measurements during the dynamic experiments. The natural frequency of the transducers was 3.6 kHz, above which the force transducer will act to attenuate oscillations. The friction experiments involved steady speeds or gradual accelerations, so high frequency dynamics were not of concern. Additionally, the experiments only used a sampling frequency of 1 kHz.

Sensor noise and drift

Measurements from piezoelectric force transducers at constant load were observed to have a standard deviation of about 0.13 N. The specified repeatability of the charge amplifiers was 0.1 N. This represents 0.5% of the normal force range (26 N) measured during the friction experiments.

The force transducers and charge amplifiers were determined to have a drift of up to 0.1 N/s after about an hour of warm-up. For each individual sensor, the drift was determined to remain consistent over several minutes. Drift was compensated by taking measurements while the apparatus was at rest for 10 s before initiating motion in order to measure the drift of each sensor. The estimated drift was then applied against the measurements.

Speed

The motors, sensors, and computer equipment generated a large amount of electromagnetic interference (EMI) that created a significant amount of drift in the timer card that performed data capture for the linear encoder. Proper grounding and shielding of cables did not do enough to remove this interference. The bandwidth of the encoder was therefore limited so that the high-frequency EMI would be ignored. Unfortunately, this meant that position measurements were constrained to motions of less than 6 mm/s before the encoder bandwidth would saturate, limiting the range for which the experiments could be conducted.

Temperature and humidity

Experiments were not conducted in a temperature controlled area. Ambient air temperatures and relative humidities were recorded for each experiment, and were found to be within $21.9 - 23.4°C$ and $24 - 30\%$, respectively. Typically, temperature did not vary by more than $0.2°$ over a single set of experiments.

Measuring equipment responds to changes in temperature typically through scale error. The linear encoder glass scale had a total growth of about $0.001\%/1°C$, or about 10 nm over 1 mm of travel, which is negligible. Force transducers had a temperature sensitivity of $0.02\%/°C$, which is negligible when compared to other force measurement errors.

Chapter 6

Conclusions and Future Research

6.1 Conclusions

6.1.1 Normal Contact

A volumetric contact dynamics model based on the Winkler elastic foundation model is presented for validation. Forces are expressed in terms of the properties of the volume of interference between the solid geometries of the bodies in contact.

A series of experiments and an apparatus have been presented to validate the model of the normal contact force in static and dynamic conditions and to identify volumetric stiffness and hysteretic damping factors. Experiments were performed using a spherical specimen on a planar surface in order to compare with more commonly used Hertzian models. A cylindrical specimen was also tested on a planar surface in order to provide a relatively large contact surface area and so that the relationship between volume of interference and measured displacement should be linear according to the model. Contact surfaces of magnesium alloy and aluminum were used against stainless steel specimens.

Quasi-static experiments were used to determine and validate Hertzian and volumetric stiffness. For spherical specimen experiments, Hertzian stiffnesses were about 2/3 of theoretical values, which is reasonable given that surface asperities tend to reduce measured contact stiffness. Volumetric stiffnesses were determined to be 3.82×10^{13} N/m^3 and 7.59×10^{13} N/m^3 for magnesium and aluminum, respectively. For the cylindrical specimen,

assuming perpendicular contact resulted in volumetric stiffness estimates several orders of magnitude lower than with the spherical specimens or theoretical values. Using stiffnesses determined from classical elastic theory, small misalignments in the apparatus were estimated that corresponded well with measured results. Partial contact with an off-angle cylinder has no classical elastic theory solution, so this demonstrates the applicability of the volumetric model to unusual geometries.

Damping experiments were also performed with the spherical specimen to measure hysteretic damping. As anticipated, contact forces increased with greater impact speed. The hysteretic damping for the volumetric model was determined to be inversely related to impact speed. For this constrained motion where the specimen is driven by the linear motor, the coefficient of restitution then remains constant.

6.1.2 Friction Contact

A seven-parameter bristle-friction model is also presented for validation. This model accounts for slip-stick transitions and dwell-time dependent effects. For bodies rotating relative to each other about the normal, the moments caused by friction across the contact surface area can be integrated to give a spinning friction torque. Additionally, the Contensou effect is modelled, where spinning friction can 'cancel out' some friction forces that would normally resist tangential motion (as with a floor polishing machine).

Experiments to validate this friction model are described. These experiments separate tangential and rotational motion in order to identify coefficients of friction, bristle dynamics, and dwell-time dependency, and combine motions to investigate the Contensou effect. An apparatus to conduct these experiments was designed and built. Experiments were conducted with the flat end of an aluminum cylinder on a titanium plane.

The weight on the specimen was determined to be excessive, as moving it produced significant wear to the contact surfaces. Friction measurements at stick-slip transition were observed to be lower than during slipping during experiments designed for tangential motion only. However, the specimen was observed to rotate slightly as it began to move. Using the angular velocity measurements, the reduction in friction force at stick-slip transition was found to correspond with what was predicted by the Contensou factors in the model. Estimates for the static coefficient of friction μ_s averaged 0.2 and ranged from 0.17

to 0.26. Bristle stiffness and damping parameters were estimated at 4500 m^{-1} and 300 s/m, respectively.

The specimen was driven at tangential speeds of 0.5 — 2.5 mm/s and the mean kinetic coefficient of friction μ_k was measured to be 0.2. Since measurements for both static and kinetic friction are both similar and highly variable (likely due to wear), the point of transition from static to kinetic friction was not found, and thus an estimate for the Stribeck velocity could not be made.

Experiments with sinusoidal motions were also conducted to investigate dwell-time dependency of the stiction force. Instead of decreasing after the first oscillation, the maximum friction force doubled over several oscillations. This adhesion effect occurred for several different frequencies, and is likely a consequence of the heat generated by metal moving repeatedly over a small area.

As the tangential experiments made a linear wear pattern in the contact surface, rotation experiments created a circular wear pattern. Static and kinetic coefficients of friction were determined to be similar for rotation as for translation. The resolution of the instruments was insufficient to estimate bristle dynamics parameters to compare with the tangential model.

To evaluate the model's characterization of the Contensou effect, the specimen was driven at constant tangential velocity with accelerating angular velocity. The model accurately accounted for the decline in the friction force. The model for spinning friction torque also correlated well with the measured results, except during periods where the angular speed was seen to change rapidly.

6.2 Future Research

The volumetric friction model has been described and validated experimentally. While these experiments demonstrate several aspects of the model, there are several improvements that can be made in order to better estimate parameters and observe phenomena described by the model.

The normal force experiments were limited by the force range of the apparatus. This limitation stemmed from the encoder reference plate deflecting away from the encoder

when a large amount of pressure was applied to the contact surface. A different position measurement solution, such as a laser interferometer, might be better suited to this application so that the deformation of the contact plate does not move the encoder reference. This would enable testing at higher normal force loads.

Improved alignment with the contact surface for the cylindrical specimens is required in order to test contact with a large flat surface area. This would enable demonstration of the model for large contact patches where point-contact models cannot easily be applied. Close alignment would be guaranteed if the specimen were mounted with a flexible coupling, though the stiffness of that coupling would require accurate characterization to ensure the integrity of position measurements for the specimen.

All of the impact experiments took place while under constrained motion from the ballscrew linear motor. As the specimen could not bounce off the contact surface, the concept of a coefficient of restitution was physically meaningless. Experiments should be performed with the specimen decoupled from the actuator and driven freely into the contact surface.

The speeds of the damping and dynamic friction experiments were limited by the bandwidth of the linear encoder, as higher bandwidths were very susceptible to EMI from the other instruments. Lower resolution encoders would enable faster speeds to be measured for the same bandwidth and should be used for higher-speed impact and friction experiments.

One aspect of the model not yet investigated experimentally is rolling resistance torque. This could be validated by taking a cylinder or sphere with known volumetric contact properties (stiffness and damping) and rolling it on a level plane until it comes to rest. The amount of deceleration could be measured and compared with the torque predicted by the model.

When the normal force of the volumetric contact model is compared directly with normal forces of classical elastic models, it appears that the volumetric stiffness parameter can be described in terms of its elastic properties and is inversely related to the radius of the contact area. Of course, the volumetric stiffness is intended to be independent of the specific geometry of contact, but it may be possible to adapt the model if the stiffness can be described in terms of the other volumetric properties already being generated for simulation, such as radius of gyration. Further investigation of this relationship is recommended.

From the friction experiments, it is apparent that the weight of the rotary motor on

the specimen is excessive and leads to significant wear. Contact pressure could be further reduced with a smaller motor, partially supporting the weight of the motor, or a significantly larger specimen (and contact plate). With less wear, the contact surfaces would not be changing and more repeatable measurements for static and kinetic friction coefficients may be obtained. If static and kinetic friction coefficients can be distinguished, then a value for the Stribeck velocity may be estimated.

The unusual adhesion effect observed during the dwell-time dependency experiments is not accounted for in the volumetric friction model. This merits further investigation. It also merits further investigation of dwell-time dependency as this phenomena was not observed in the experiments.

For the tangential motion experiments, a fixed orientation of the specimen is required so that stick-slip transition can be observed without being influenced by the Contensou effect. This should also lead to more reliable estimates of maximum static friction.

Sensitivity analysis of parameters identified for the model and investigation of other methods of online and offline system identification is recommended.

Finally, now that an apparatus and framework have been developed for contact dynamics experiments, more geometries and materials should be tested in order to develop a database of material contact properties for the volumetric model.

References

[1] Y. Gonthier, *Contact Dynamics Modelling for Robotic Task Simulation*. PhD thesis, University of Waterloo, 2007.

[2] Y. Gonthier, J. McPhee, and C. Lange, "On the implementation of coulomb friction in a volumetric-based model for contact dynamics," *ASME Design Engineering Technical Conferences and 6th International Conference on Multibody Systems, Nonlinear Dynamics and Control*, September 2007.

[3] Y. Gonthier, J. McPhee, C. Lange, and J.-C. Piedbœuf, "A contact modeling method based on volumetric properties," *ASME Design Engineering Technical Conferences and 5th International Conference on Multibody Systems, Nonlinear Dynamics and Control*, pp. 477–486, 2005.

[4] J. de Carufel, E. Martin, and J.-C. Piedbœuf, "Control strategies for hardware-in-the-loop simulation of flexible space robots," *IEEE Proceedings-D: Control Theory and Applications*, vol. 147, no. 6, pp. 569–579, 2000.

[5] Y. Gonthier, J. McPhee, C. Lange, and J.-C. Piedbœuf, "A regularized contact model with asymmetric damping and dwell-time dependent friction," *Multibody System Dynamics*, vol. 11, no. 3, pp. 209–233, 2004.

[6] F. Janabi-Sharifi, "Collision: Modeling, simulation and identification of robotic manipulators interacting with environments," *Journal of Intelligent and Robotic Systems*, vol. 13, pp. 1–44, May 1995.

[7] D. Marhefka and D. Orin, "A compliant contact model with nonlinear damping for simulation of robotic systems," *Systems, Man and Cybernetics, Part A: Systems and Humans*, vol. 29, pp. 566–572, November 1999.

[8] H. M. Lankarani and P. E. Nikravesh, "Continuous contact force models for impact analysis in multibody systems," *Nonlinear Dynamics*, vol. 5, pp. 193–207, 1994.

[9] K. Hunt and F. Crossley, "Coefficient of restitution interpreted as damping in vibroimpact," *Journal of Applied Mechanics*, vol. 7, pp. 440–445, June 1975.

[10] W. Goldsmith, *Impact: The Theory and Physical Behavior of Colliding Solids*. London, U.K.: Edward Arnold Ltd., 1960.

[11] Y. Khulief and A. Shabana, "A continuous force model for the impact analysis of flexible multibody systems," *Mechanism and machine theory*, vol. 22, no. 3, pp. 213–224, 1987.

[12] G. Gilardi and I. Sharf, "Literature survey of contact dynamics modelling," *Mechanism and Machine Theory*, vol. 37, pp. 1213–1239, 2002.

[13] E. Rabinowicz, "Stick and slip," *Scientific American*, vol. 194, no. 5, pp. 109–118, 1956.

[14] K. Arakawa and E. Krotkov, "Estimating fractal dimension of natural terrain from irregularly spaced data," in *IEEE/RSJ International Workshop on Intelligent Robots and Systems*, pp. 1364–1370, July 1993.

[15] A. R. Bailey and R. S. Sayles, "Effect of roughness and sliding friction on contact stresses," *ASME Journal of Tribology*, vol. 113, pp. 729–738, Oct. 1991.

[16] B. Armstrong-Hélouvry, P. Dupont, and C. C. De Wit, "A survey of models, analysis tools and compensation methods for the control of machines with friction," *Automatica*, pp. 1083–1138, July 1994.

[17] P. Contensou, "Couplage entre frottement de glissement et frottement de pivotement dans la théorie de la toupie," in *Kreiselprobleme und Gyrodynamics* (H. Ziegler, ed.), IUTAM Symposium Celerina, 1962, pp. 201–216, Springer-Verlag, Berlin, 1963.

[18] K. Johnson, *Contact Mechanics*. London: Cambridge University Press, 1985.

[19] M. Weber, O. Ma, and I. Sharf, "Identification of contact dynamics model parameters from contstrained robotic operations," in *Proceedings of DETC'02 ASME 2002 Design*

Engineering Technical Conferences and Computer and Information in Engineering Conference, (Montreal, Canada), Sept. 29–Oct. 2 2002. DETC2002/MECH-34357.

[20] J. Agar, I. Sharf, C. Lange, and Y. Gonthier, "Contact parameter estimation with a space robot verification facility," *ASME Design Engineering Technical Conferences and 5th International Conference on Multibody Systems, Nonlinear Dynamics and Control*, pp. 433–442, 2005.

[21] N. Diolaiti, C. Melchiorri, and S. Stramigioli, "Contact impedance estimation for robotic systems," *IEEE Transactions on Robotics*, vol. 21, pp. 925–935, Oct. 2005.

[22] D. Verscheure, I. Sharf, H. Bruyninckx, J. Swevers, and J. D. Schutter, "Identification of contact dynamics parameters for stiff robotic payloads," *IEEE Transactions on Robotics*, vol. 25, pp. 240–252, April 2009.

[23] J. Liang, S. Fillmore, and O. Ma, "A 2d bristle friction force model for general contact dynamics simulation," in *The 1st Joint International Conference on Multibody System Dynamics*, May 2010.

[24] E. P. Popov, *Engineering Mechanics of Solids*. Upper Saddle River, New Jersey: Prentice Hall, 2nd ed., 1998.

[25] J. W. Harris and H. Stocker, *Handbook of Mathematics and Computational Science*, pp. 104, 107. New York: Springer-Verlag, 1998.

[26] I. N. Sneddon, "The relation between load and penetration in the axisymmetric Boussinesq problem for a punch of arbitrary profile," *International Journal of Engineering Science*, vol. 3, no. 1, pp. 47 – 57, 1965.

[27] R. L. Munisamy, D. A. Hills, and D. Nowell, "The solution of the contact between a tilted circular rigid punch and an elastic half-space," *Wear*, vol. 184, no. 1, pp. 93 – 95, 1995.

[28] M. Bahrami, M. M. Yovanovich, and J. R. Culham, "A compact model for spherical rough contacts," *Journal of Tribology*, vol. 127, pp. 884–889, Oct. 2005.

APPENDICES

Appendix A

Equipment Specifications

The following tables list the software and equipment used as part of the contact dynamics experimental apparatus.

Vendor	Package	Version
Kollmorgen	S200 OC Tools	3.0.0
Kollmorgen	DriveGUI	2.00_0074
National Instruments	LabVIEW with RealTime Module	8.5
National Instruments	Measurement and Automation Explorer	8.5
Kistler	ManuWare	1.0

Table A.1: Software.

Vendor	Part	Description
National Instruments	PXI-1042Q	8-Slot PXI Chassis
National Instruments	PXI-8106	Controller with RealTime Embedded SW
Dell	Optiplex 760	Desktop computer

Table A.2: Computer hardware.

Vendor	Part	Description
Kollmorgen	AKM43	DC Brushless Servo Motor
Kollmorgen	S30661	DC Brushless Servo Drive 6 A
Kollmorgen	2RB12G0N0262	Ball-Screw Linear Actuator
Kollmorgen	AKM23C	DC Brushless Servo Motor
Kollmorgen	S20260	DC Brushless Servo Drive 1.5 A
National Instruments	PXI-7342	2-Axis Stepper/Servo Motion Controller
National Instruments	UMI-7772	Universal Motion Interface

Table A.3: Actuation equipment.

Vendor	Part	Description	Quantity
Kistler	9347	3-Component Force Link 5 kN	2
Kistler	5073A311	3-Channel Charge Amplifier	2
National Instruments	PXI-6123	Multifunction DAQ Device	1
MicroE Systems	MII4800	Linear Encoder 1.2 nm	1
MicroE Systems	MIIL130	Glass Linear Reference Grating	1
National Instruments	PXI-6602	Counter/Timer DAQ Device	1

Table A.4: Measurement equipment.